47th AIAA Aerospace Sciences Meeting Including The New Horizons Forum and Aerospace Exposition
5 - 8 January 2009, Orlando, Florida

AIAA 2009-1507

Detached-Eddy Simulation of Transonic Limit Cycle Oscillations Using High Order Schemes

Baoyuan Wang[*], Ge-Cheng Zha[†]
Dept. of Mechanical and Aerospace Engineering
Miami Wind^{TM}
University of Miami
Coral Gables, Florida 33124
E-mail: gzha@miami.edu

Abstract

This paper is to investigate the flow non-linearity of the fluid-structural interaction using detached eddy simulation (DES) of turbulence. A low diffusion E-CUSP (LDE) scheme with 5th order WENO scheme is employed to calculate the inviscid fluxes. A fully conservative 4th order central differencing is used for the viscous terms. A fully coupled fluid-structural model is employed. The limited cycle oscillation (LCO) of the NLR7301 airfoil is simulated in 2D using RANS method and in 3D using DES method. For the cases computed in this paper, the predicted LCO frequency, amplitudes, averaged lift and moment, all agree excellently with the experiment. The solutions appear to have bifurcation and are dependent on the initial fields or initial perturbation. The developed computational fluid dynamics (CFD)/computational structure dynamics (CSD) simulation is able to capture the LCO with very small amplitudes measured in the experiment. This is attributed to the high order low diffusion schemes, fully coupled FSI model, and the turbulence model used. This research appears to be the first time that a numerical simulation of LCO matches the experiment. The simulation confirms several observations of the experiment.

1 Introduction

Flow induced structural vibration is one of the most challenging problems affecting the military and commercial aircraft. Due to the complicated non-linear fluid-structural interaction phenomena, there is a lack of high fidelity computational tools to study the basic physics and to accurately predict the structural failure. For airframe, there are the problems such as transonic flutter, limit cycle oscillation, buzz, buffet, etc. For propulsion turbomachinery, there are the problems such as high cycle fatigue caused by forced response or stall flutter, etc. Helicopter rotor blades constantly work under the vibration induced by blade wake and tip vortexes. Development of advanced methodologies to accurately simulate fluid-structural interactions hence will have broad impact on improving the performance of various aircraft.

---

[*] Ph.D Candidate

[†] Associate Professor, AIAA Senior Member, Director of Miami Wind^{TM}

Copyright © 2009 by all the authors of this paper. Published by the American Institute of Aeronautics and Astronautics, Inc., with permission.

The difficult issue that the fluid-structural interaction community currently faces is the non-linearity caused by both fluid and structure. The aerodynamic non-linearity poses more challenge than the structural one[1, 2]. These problems are often accompanied or caused by the complicated flow phenomena such as shock wave/turbulent boundary layer interaction, flow separation, vortex shedding, etc.

Many efforts have been made by solving the time accurate Euler or Navier-Stokes equations in time domain with loosely or fully coupled linear or non-linear structural models to study the nonlinear fluid-structural interaction problems. Bendiksen et al.[3] pioneered the research by using an explicit CFD code coupled with a structural integrator based on the convolution integral to obtain the flutter boundary for a NACA 64A010 airfoil. The loosely coupled models between fluid and structural solvers include the work of Guruswamy[4], Lee-Rausch et al.[5], Smith[6], Vermeersch et al.[7], Darracq, et al.[8], Prananta, et al.[9], Bohbot et al.[10], and Blom et al.[11]. Alonso and Jameson developed a model which is close to the fully coupled method with the structural displacement updated every several fluid solver iterations[12]. The implicit Runge-Kutta method with multigrid acceleration is employed for the flow solver in Alonso's work[12][13]. In 1997-98, Morton and Melville et al. developed a implicit fully coupled fluid structural interaction model, which used the Beam-Warming implicit scheme for the flow solver coupled with modal structural solver [14][15][16]. In 2001, Liu et al. developed a fully coupled method using Jameson's explicit scheme with multigrid method and a finite element structural model [17]. In 2004-2005, Chen and Zha et al. developed a fully coupled fluid-structural interaction methodology using implicit Gauss-Seidel iteration, which does not have the factorization error of the Beam-Warming implicit method and hence allows larger time step[18, **?**, 19].

However, the results form the time domain time accurate nonlinear flow solver have not yielded more optimistic results. In general, the weak divergence, flutter divergence and onset of LCO can be captured and predicted quite well, but the amplitude of LCO is still over predicted. These can be seen in the work by Bendiksen[2], Morton and Beran[20], Weber et al.[21], and Tang at al.[1]. Even though the inviscid Euler solver can capture the onset of LCO, the viscous Navier-Stokes solvers predict the LCO amplitude closer to experiments than the Euler solver. The LCO amplitude is also dependent on the turbulence model used as pointed out by Tang et al.[1] when the NLR 7301 airfoil is calculated[22, 23]. The non-linear structural model does not produce better results of LCO as reported by Gordnier in 2003[24]. The calculation with wind tunnel wall porosity yields better LCO amplitude, but a significant difference remains if the actual wind tunnel wall porosity is used (Castro et al., 2001)[25].

According to Bendiksen[2], both the LCO and transonic dip may be caused by aerodynamic non-linearity due to shock wave/turbulent boundary layer interaction and the resulted separation. The experiments of Schewe and Dietz et al. in 2003 and 2004 [22, 23] for the NLR 7301 supercritical airfoil tend to support this hypothesis even though there was no clear evidence that the flow separation occurs with the very small LCO amplitude. Schewe et al. [22] attribute two nonlinearity mechanisms to the amplitude-limiting phenomenon: 1)the oscillating shock strength and the coupled pulsations of the marginally separated flow beneath the shock; 2) the trailing edge separation they deduced from the significant increase in the r.m.s. value of the pressure fluctuation near trailing edge.

Schewe et al. [22] gave the following important observations and questions: First, the LCOs they captured have very small relative amplitudes of the plunge on the order of 2/1000 to 3/1000 of the chord and the pitching amplitude of 1° - 2°. They questioned if the LCOs of such small amplitudes are the artefacts of the wind-tunnel experiment or could also occur in the unbounded flow. Second, all the reported numerical simulations at that time only captured the much greater LCO amplitudes.

They questioned if it means the co-existence of multiple LCOs at constant flow conditions. They found that the multiple coexisting LCOs in their experiments. Third, they observed that the wall boundary layer transition from laminar to turbulent does not have much effect on LCO. Fourth, they observed that the wind tunnel wall interference with or without perforated test section does not have much effect on LCOs. Fifth, they observed that the transition from steady to oscillatory state can be either continuous or discontinuous.

To resolve the aerodynamic non-linearity such as shock wave/turbulent boundary layer interaction and flow separation, the turbulence simulation is critical. All the research mentioned above are based on Reynolds averaged Navier-Stokes equations(RANS). However, RANS models are known to be not able to calculate the flow separation correctly. RANS methods intend to model the large scale eddies using a universal model. Large scale turbulence is affected by the flow geometry and boundary conditions and a universal model does not exist.

Large Eddy Simulation (LES) is promising to overcome the disadvantages of the RANS model. In LES, the governing equations are spatially filtered on the scale of the numerical grid. The large energy containing scales are directly simulated, and the small scale eddies, which are generally more homogeneous and universal, are modeled. The large eddies are strongly affected by the flow field geometry boundaries. Therefore the direct computation of the large eddies by LES is more accurate than the modeling of the large eddies by RANS. However, for high Reynolds number flows such as those of transonic wings and turbomachinery blades, to resolve the wall boundary layer, LES needs the CPU resource not much less than the Direct Numerical Simulation(DNS). This makes the LES too expensive for fluid-structural interaction unsteady calculations. For engineering applications, it is not hopeful for LES to be rigorously used until in another 4 decades[26].

To overcome the intensive CPU requirement for LES, Spalart et al. developed the detached eddy simulation (DES) strategy[26], which is a hybrid RANS and LES method. Near the solid surface within the wall boundary layer, the unsteady RANS model is realized. Away from the wall surface, the model automatically converts to LES. By using the RANS model near walls, the mesh size as well as the CPU time can be tremendously reduced. The motivation of DES is that the LES is powerful in regions of massive separation and other free shear flows such as jets, but much too costly in the large area of thin wall boundary layers.

Spalart gave a grid guidance for DES in 2001[27, 28], which divides a flow domain with solid walls to Euler region, RANS region, and LES region. In the RANS region, the domain is further divided to Viscous region and Outer region. The LES region is composed of Viscous, Focus and Departure region. Spalart's DES grid guidance give sufficient grid resolution for LES region and the transition to Euler region and from RANS region. The grid size is dramatically reduced compared to the pure LES.

Even though DES concept is much newer than RANS and LES concept, its application for turbulence simulation has already achieved encouraging success as shown in the work of Tarvin et al. (1999) [29], Spalart (2001)[27, 28], Forsythe et al.(2002)[30], Viswanathan et al. [31], Squires et al.[32, 33], Hsnsen, et al. (2003)[34], Subbareddy et al. (2005) [35] and Wang et al. (2008) [36]. These flows calculated using DES include those for airfoils, cylinders, forbodies, base flows, etc. The results are qualitatively and quantitatively better than the solutions using RANS. DES appears to be a suitable compromise between the physical models of turbulence and CPU efficiency.

Most of the calculations of fluid-structural interaction today employ 2nd order accuracy in both space and time. The shock wave/boundary layer interaction is considered as the critical factor affecting the non-linearity transonic airfoil LCO[22]. It is hence very important to have a high resolution low diffusion shock capturing scheme to resolve the shock boundary layer interaction. The WENO scheme is a desirable candidate since it can achieve uniformly high order accuracy up to the shock discontinuities. In addition, the low diffusion of the numerical scheme is critical to accurately predict the flow damping, which may significantly affect the structure displacement.

The objective of this research is to simulate the challenging nonlinear LCO phenomenon with high fidelity numerical algorithms, which include high order (5th order) WENO scheme[37, 38], a low diffusion E-CUSP (LDE) Riemann solver[39, 40], a new 4th order fully conservative central differencing scheme for viscous terms[38], an implicit 2nd order accuracy time marching scheme with Gauss-Seidel line relaxation, a fully coupled fluid-structural interaction model[18, **?**, 19], advanced Spalart-Allmaras (S-A) one-equation RANS turbulence model[41], and the Spalart's DES turbulence modeling[26].

The rigorous efforts of this research appear to be paid off with the numerical simulation matching the experiment excellently for the first time. This simulation also confirms some of the experimental observations and answers some important questions. First, the LCOs with the small relative amplitude is captured with unbounded flows in the numerical simulation. This means they should not be the artefacts of the wind-tunnel experiment and most likely are the factual phenomenon. Second, the co-existence of multiple LCOs at constant flow conditions is confirmed in our simulation. The reason that other numerical simulations only capture the LCOs with large amplitudes may be due to their high numerical dissipation that either smears out the small amplitude LCO or is only able to resolve the large amplitudes LCOs. Third, the numerical simulation of this research confirms that the wall boundary layer transition from laminar to turbulent does not have a large effect on LCOs at high Reynolds number, because our simulation assumes that the boundary layer is fully turbulent from the airfoil leading edge. Fourth, the simulation confirms that the wind tunnel wall interference with or without perforated test section does not have much effect on LCOs because our simulation uses the unbounded flow condition with no wind tunnel wall effect at all. Fifth, the numerically captured LCO is not accompanied with any flow separation due to the very small amplitude. This may rectify the hypothesis that the LCOs are caused by the nonlinearity of flow separation induced by shock/boundary layer interaction. In other words, the nonlinearity of shock/boundary layer interaction with no flow separation is sufficient to trigger a LCO. This may make reduced numerical models feasible to capture LCOs.

In this paper, the Spalart-Allmaras one-equation RANS turbulence model is used first to search the LCO since the RANS model is conducted as 2D simulation and is much more efficient than the 3D DES. The DES then uses the parameters searched by the RANS model to save CPU time. The DES simulation is already very close to the experiment as of writing this paper and the final result will be reported soon.

2 Governing Equations

The governing equations for the flow field computation are the spatially filtered 3D general Navier-Stokes equations in generalized coordinates and can be expressed as the following:

$$\frac{\partial \mathbf{Q}'}{\partial t} + \frac{\partial \mathbf{E}'}{\partial \xi} + \frac{\partial \mathbf{F}'}{\partial \eta} + \frac{\partial \mathbf{G}'}{\partial \zeta} = \frac{1}{\mathrm{Re}}\left(\frac{\partial \mathbf{E}'_{\mathbf{v}}}{\partial \xi} + \frac{\partial \mathbf{F}'_{\mathbf{v}}}{\partial \eta} + \frac{\partial \mathbf{G}'_{\mathbf{v}}}{\partial \zeta}\right) \tag{1}$$

where Re is the Reynolds number, and

$$\mathbf{Q}' = \frac{\mathbf{Q}}{J} \tag{2}$$

$$\mathbf{E}' = \frac{1}{J}(\xi_t\mathbf{Q} + \xi_x\mathbf{E} + \xi_y\mathbf{F} + \xi_z\mathbf{G}) \tag{3}$$

$$\mathbf{F}' = \frac{1}{J}(\eta_t\mathbf{Q} + \eta_x\mathbf{E} + \eta_y\mathbf{F} + \eta_z\mathbf{G}) \tag{4}$$

$$\mathbf{G}' = \frac{1}{J}(\zeta_t\mathbf{Q} + \zeta_x\mathbf{E} + \zeta_y\mathbf{F} + \zeta_z\mathbf{G}) \tag{5}$$

$$\mathbf{E_v}' = \frac{1}{J}(\xi_x\mathbf{E_v} + \xi_y\mathbf{F_v} + \xi_z\mathbf{G_v}) \tag{6}$$

$$\mathbf{F_v}' = \frac{1}{J}(\eta_x\mathbf{E_v} + \eta_y\mathbf{F_v} + \eta_z\mathbf{G_v}) \tag{7}$$

$$\mathbf{G_v}' = \frac{1}{J}(\zeta_x\mathbf{E_v} + \zeta_y\mathbf{F_v} + \zeta_z\mathbf{G_v}) \tag{8}$$

where J is the transformation Jacobian. The variable vector $\mathbf{Q}$, and inviscid flux vectors $\mathbf{E}$, $\mathbf{F}$, and $\mathbf{G}$ are given as the following.

$$\mathbf{Q} = \begin{pmatrix} \bar{\rho} \\ \bar{\rho}\tilde{u} \\ \bar{\rho}\tilde{v} \\ \bar{\rho}\tilde{w} \\ \bar{\rho}\tilde{e} \end{pmatrix}, \mathbf{E} = \begin{pmatrix} \bar{\rho}\tilde{u} \\ \bar{\rho}\tilde{u}^2 + \bar{p} \\ \bar{\rho}\tilde{u}\tilde{v} \\ \bar{\rho}\tilde{u}\tilde{w} \\ (\bar{\rho}\tilde{e} + \bar{p})\tilde{u} \end{pmatrix}, \mathbf{F} = \begin{pmatrix} \bar{\rho}\tilde{v} \\ \bar{\rho}\tilde{v}\tilde{u} \\ \bar{\rho}\tilde{v}^2 + \bar{p} \\ \bar{\rho}\tilde{v}\tilde{w} \\ (\bar{\rho}\tilde{e} + \bar{p})\tilde{v} \end{pmatrix}, \mathbf{G} = \begin{pmatrix} \bar{\rho}\tilde{w} \\ \bar{\rho}\tilde{w}\tilde{u} \\ \bar{\rho}\tilde{w}\tilde{v} \\ \bar{\rho}\tilde{w}^2 + \bar{p} \\ (\bar{\rho}\tilde{e} + \bar{p})\tilde{w} \end{pmatrix}$$

The inviscid fluxes in generalized coordinate system are expressed as:

$$\mathbf{E}' = \begin{bmatrix} \bar{\rho}U \\ \bar{\rho}\tilde{u}U + l_x\bar{p} \\ \bar{\rho}\tilde{v}U + l_y\bar{p} \\ \bar{\rho}\tilde{w}U + l_z\bar{p} \\ (\bar{\rho}\tilde{e} + \bar{p})\,U - l_t\bar{p} \end{bmatrix}, \mathbf{F}' = \begin{bmatrix} \bar{\rho}V \\ \bar{\rho}\tilde{u}V + m_x\bar{p} \\ \bar{\rho}\tilde{v}V + m_y\bar{p} \\ \bar{\rho}\tilde{w}V + m_z\bar{p} \\ (\bar{\rho}\tilde{e} + \bar{p})\,V - m_t\bar{p} \end{bmatrix}, \mathbf{G}' = \begin{bmatrix} \bar{\rho}W \\ \bar{\rho}\tilde{u}W + n_x\bar{p} \\ \bar{\rho}\tilde{v}W + n_y\bar{p} \\ \bar{\rho}\tilde{w}W + n_z\bar{p} \\ (\bar{\rho}\tilde{e} + \bar{p})\,W - n_t\bar{p} \end{bmatrix}$$

where U, V and W are the contravariant velocities in ξ, η and ζ directions.

$$\begin{aligned} U &= l_t + \mathbf{l} \bullet \mathbf{V} = l_t + l_x\tilde{u} + l_y\tilde{v} + l_z\tilde{w} \\ V &= m_t + \mathbf{m} \bullet \mathbf{V} = m_t + m_x\tilde{u} + m_y\tilde{v} + m_z\tilde{w} \\ W &= n_t + \mathbf{n} \bullet \mathbf{V} = n_t + n_x\tilde{u} + n_y\tilde{v} + n_z\tilde{w} \end{aligned} \tag{9}$$

$\mathbf{l}$, $\mathbf{m}$, $\mathbf{n}$ are the normal vectors on ξ, η, ζ surfaces with their magnitudes equal to the elemental surface area and pointing to the directions of increasing ξ, η, ζ.

$$\mathbf{l} = \frac{\nabla\xi}{J},\ \mathbf{m} = \frac{\nabla\eta}{J},\ \mathbf{n} = \frac{\nabla\zeta}{J} \tag{10}$$

$$l_t = \frac{\xi_t}{J},\ m_t = \frac{\eta_t}{J},\ n_t = \frac{\zeta_t}{J} \tag{11}$$

The viscous fluxes $\mathbf{E_v}$, $\mathbf{F_v}$, $\mathbf{G_v}$ are expressed as:

$$\mathbf{E_v} = \begin{pmatrix} 0 \\ \bar{\tau}_{xx} + \sigma_{xx} \\ \bar{\tau}_{xy} + \sigma_{xy} \\ \bar{\tau}_{xz} + \sigma_{xz} \\ Q_x \end{pmatrix},\ \mathbf{F_v} = \begin{pmatrix} 0 \\ \bar{\tau}_{yx} + \sigma_{yx} \\ \bar{\tau}_{yy} + \sigma_{yy} \\ \bar{\tau}_{yz} + \sigma_{yz} \\ Q_y \end{pmatrix},\ \mathbf{G_v} = \begin{pmatrix} 0 \\ \bar{\tau}_{zx} + \sigma_{zx} \\ \bar{\tau}_{zy} + \sigma_{zy} \\ \bar{\tau}_{zz} + \sigma_{zz} \\ Q_z \end{pmatrix},$$

The overbar denotes a regular filtered variable, and the tilde is used to denote the Favre filtered variable. In above equations, ρ is the density, u, v, w are the Cartesian velocity components in x, y, z directions, p is the static pressure, and e is the total energy per unit mass.

The $\bar{\tau}$ is the molecular viscous stress tensor and is estimated as:

$$\bar{\tau}_{ij} = \frac{2}{3}\tilde{\mu}\frac{\partial \tilde{u}_k}{\partial x_k}\delta_{ij} + \tilde{\mu}\left(\frac{\partial \tilde{u}_i}{\partial x_j} + \frac{\partial \tilde{u}_j}{\partial x_i}\right), \qquad i, j = 1, 2, 3 \tag{12}$$

The above equation is in tensor form, where the subscript 1, 2, 3 represent the coordinates, x, y, z, and the Einstein summation convention is used.

The molecular viscosity $\tilde{\mu} = \tilde{\mu}(\tilde{T})$ is determined by Sutherland law.

The σ is the subgrid scale stress tensor due to the filtering process and is expressed as:

$$\sigma_{ij} = -\bar{\rho}(\widetilde{u_i u_j} - \tilde{u}_i \tilde{u}_j) \tag{13}$$

The energy flux Q is expressed as:

$$Q_i = \tilde{u}_j(\bar{\tau}_{ij} + \sigma_{ij}) - \bar{q}_i + \Phi_i \tag{14}$$

where Φ is the subscale heat flux:

$$\Phi_i = -C_p\bar{\rho}(\widetilde{u_i T} - \tilde{u}_i \tilde{T}) \tag{15}$$

The $\bar{q}_i$ is the molecular heat flux:

$$\bar{q}_i = -\frac{C_p \tilde{\mu}}{Pr}\frac{\partial \tilde{T}}{\partial x_i} \tag{16}$$

$$\bar{\rho}\tilde{e} = \frac{\bar{p}}{(\gamma - 1)} + \frac{1}{2}\bar{\rho}(\tilde{u}^2 + \tilde{v}^2 + \tilde{w}^2) + \rho k \tag{17}$$

where γ is the ratio of specific heats, ρk is the subscale kinetic energy per unit volume.

$$\rho k = \frac{1}{2}\bar{\rho}(\widetilde{u_i u_i} - \tilde{u}_i \tilde{u}_i) = -\frac{1}{2}\sigma_{ii} \tag{18}$$

In the present calculation, the ρk in Eq.(17) is omitted based on the assumption that the effect is small.

For simplicity, all the overbar and tilde in above equations will be dropped in the rest of this paper.

3 Detached Eddy Simulation

Even though above Navier-Stokes equations are given for LES, the closure of the equations will be based on the DES model suggested by Spalart et al. [26] as the following.

$$\sigma_{ij} = \mu_{DES}(\frac{\partial \tilde{u}_i}{\partial x_j} + \frac{\partial \tilde{u}_j}{\partial x_i} - \frac{2}{3}\frac{\partial \tilde{u}_k}{\partial x_{\ k}}\delta_{ij}) - \frac{2}{3}\rho k \delta_{ij} \qquad i,j = 1,2,3 \tag{19}$$

The turbulent heat flux will be evaluated as:

$$\Phi_i = C_p \frac{\mu_{DES}}{Pr_t}\frac{\partial \tilde{T}}{\partial x_i} \tag{20}$$

Where

$$\mu_{DES} = \rho \nu_t = \rho \tilde{\nu} f_{v1} \tag{21}$$

$\tilde{\nu}$ is a working variable and is determined by the following Spalart-Allmaras model[41][26][31][42]:

$$\frac{D\tilde{\nu}}{Dt} = c_{b1}\tilde{S}\tilde{\nu} - [c_{w1}f_w - \frac{c_{b1}}{k^2}f_{t2}][\frac{\tilde{\nu}}{d}]^2 + \frac{1}{\sigma}[\nabla \cdot ((\nu + \tilde{\nu})\nabla\tilde{\nu}) + c_{b2}(\nabla\tilde{\nu})^2] \tag{22}$$

The eddy viscosity ν_t is obtained from:

$$\nu_t = \tilde{\nu} f_{v1} \qquad f_{v1} = \frac{X^3}{X^3 + c_{v1}^3} \qquad X = \frac{\tilde{\nu}}{\nu} \tag{23}$$

where ν is the molecular viscosity. The production term is:

$$\tilde{S} = S + \frac{\tilde{\nu}}{k^2 d^2} f_{v2}, \qquad f_{v2} = 1 - \frac{X}{1 + X f_{v1}} \tag{24}$$

where S is the magnitude of the vorticity. The function f_w is given by

$$f_w = g(\frac{1 + c_{w3}^6}{g^6 + c_{w3}^6})^{1/6}, \qquad g = r + c_{w2}(r^6 - r), \qquad r = \frac{\tilde{\nu}}{\tilde{S} k^2 d^2} \tag{25}$$

The values of the coefficients are: $c_{b1} = 0.1355, c_{b2} = 0.622, \sigma = \frac{2}{3}, c_{w1} = \frac{c_{b1}}{k^2} + (1 + c_{b2})/\sigma, c_{w2} = 0.3, c_{w3} = 2, k = 0.41, c_{v1} = 7.1, c_{t1} = 1.0, c_{t2} = 2.0, c_{t3} = 1.1, c_{t4} = 2.0$.

In DES, $C_{t1} = 0$, $C_{t3} = 0$. The distance to the nearest wall, d, is replaced by $\tilde{d}$ as

$$\tilde{d} = min(d, C_{DES}\Delta) \tag{26}$$

where Δ is the largest spacing of the grid cell in all the directions.

Within the boundary layer close to walls, $\tilde{d} = d$, hence the turbulence is simulated by the RANS mode determined by the Spalart-Allmaras model[41]. Away from the boundary layer, $\tilde{d} = C_{DES}\Delta$ is most of the cases. When the production and destruction terms of the model are balanced, the length scale $\tilde{d}$ will have a Smagorinsky-like eddy viscosity and the turbulence is simulated by the LES model. Analogous to the classical LES theory, the length scale Δ is to cascade the energy to the grid size. The coefficient $C_{DES} = 0.65$ is used as set in the homogeneous turbulence[43]. The Pr_t may take the value of 0.9 within the boundary layer for RANS mode and 0.5 for LES mode away from the wall surface. Eq.(22) will be extended to generalized coordinates and will be coupled and solved together with the filtered Navier-Stokes equations, Eq.(1).

4 The Numerical Method

4.1 The Low Diffusion E-CUSP (LDE) Scheme

The LDE scheme developed by Zha et al.[39] is employed to evaluate the inviscid fluxes. The basic idea of the LDE scheme is to split the inviscid flux into the convective flux E^c and the pressure flux E^p. With the one extra equation from the S-A model for DES, the splitting is basically the same as the original scheme for the Euler equation and is straightforward. This is an advantage over the Roe scheme, for which the eigenvectors need to be derived when any extra equation is added to the governing equations. Furthermore, when it is coupled with the Spalart-Allmaras one-equation model, the LDE scheme shows that it maintains high stability, whereas the stability of the Roe scheme is significantly reduced due to losing the diagonal dominance[40]. This is particularly important for DES which employs the Spalart-Allmaras one-equation model. It allows greater CFL numbers to save CPU time.

In generalized coordinate system, the flux $\mathbf{E}$ can be split as the following:

$$\mathbf{E}' = E^c + E^p = \begin{pmatrix} \rho U \\ \rho u U \\ \rho v U \\ \rho w U \\ \rho e U \\ \rho \tilde{\nu} U \end{pmatrix} + \begin{pmatrix} 0 \\ l_x p \\ l_y p \\ l_z p \\ p\overline{U} \\ 0 \end{pmatrix} \tag{27}$$

where, U is the contravariant velocity in ξ direction and is defined as the following:

$$U = l_t + l_x u + l_y v + l_z w \tag{28}$$

$\overline{U}$ is defined as:

$$\overline{U} = l_x u + l_y v + l_z w \tag{29}$$

The convective term, E^c is evaluated by

$$E^c = \rho U \begin{pmatrix} 1 \\ u \\ v \\ w \\ e \\ \tilde{\nu} \end{pmatrix} = \rho U f^c, \ f^c = \begin{pmatrix} 1 \\ u \\ v \\ w \\ e \\ \tilde{\nu} \end{pmatrix} \tag{30}$$

let

$$C = c\left(l_x^2 + l_y^2 + l_z^2\right)^{\frac{1}{2}} \tag{31}$$

where $c = \sqrt{\gamma RT}$ is the speed of sound. Then the convective flux at interface $i + \frac{1}{2}$ is evaluated as:

$$E^c_{i+\frac{1}{2}} = C_{\frac{1}{2}}\left[\rho_L C^+ f^c_L + \rho_R C^- f^c_R\right] \tag{32}$$

where, the subscripts L and R represent the left and right hand sides of the interface.

$$C_{\frac{1}{2}} = \frac{1}{2}\left(C_L + C_R\right), \ C^+ = \alpha^+_L\left(1 + \beta_L\right) M_L - \beta_L M^+_L - M^+_{\frac{1}{2}}$$

$$C^- = \alpha^-_R\left(1 + \beta_R\right) M_R - \beta_R M^-_R + M^-_{\frac{1}{2}}$$

$$M_L = \frac{U_L}{C_{\frac{1}{2}}}, \ M_R = \frac{U_R}{C_{\frac{1}{2}}}$$

$$\alpha_{L,R} = \frac{1}{2}\left[1 \pm sign\left(M_{L,R}\right)\right]$$

$$\beta_{L,R} = -max\left[0, 1 - int\left(|M_{L,R}|\right)\right]$$

$$M^+_{\frac{1}{2}} = M_{\frac{1}{2}}\frac{C_R + C_L\Phi}{C_R + C_L}, \ M^-_{\frac{1}{2}} = M_{\frac{1}{2}}\frac{C_L + C_R\Phi^{-1}}{C_R + C_L}, \ \Phi = \frac{\left(\rho C^2\right)_R}{\left(\rho C^2\right)_L}$$

$$M_{\frac{1}{2}} = \beta_L \delta^+ M^-_L - \beta_R \delta^- M^+_R$$

$$M^{\pm}_{L,R} = \pm\frac{1}{4}\left(M_{L,R} \pm 1\right)^2$$

$$\delta^{\pm} = \frac{1}{2}\left\{1 \pm sign\left[\frac{1}{2}\left(M_L + M_R\right)\right]\right\}$$

The pressure flux, E^p is evaluated as the following

$$E^p_{i+\frac{1}{2}} = \begin{pmatrix} 0 \\ \mathcal{P}^+ p\, l_x \\ \mathcal{P}^+ p\, l_y \\ \mathcal{P}^+ p\, l_z \\ \frac{1}{2}p\left[\overline{U} + \overline{C}_{\frac{1}{2}}\right] \\ 0 \end{pmatrix}_L + \begin{pmatrix} 0 \\ \mathcal{P}^- p\, l_x \\ \mathcal{P}^- p\, l_y \\ \mathcal{P}^- p\, l_z \\ \frac{1}{2}p\left[\overline{U} - \overline{C}_{\frac{1}{2}}\right] \\ 0 \end{pmatrix}_R \tag{33}$$

The contravariant speed of sound $\overline{C}$ in the pressure vector is consistent with $\overline{U}$. It is computed based on C as the following,

$$\overline{C} = C - l_t \tag{34}$$

The use of $\overline{U}$ and $\overline{C}$ instead of U and C in the pressure vector to take into account of the grid speed so that the flux will transit from subsonic to supersonic smoothly. When the grid is stationary, $l_t = 0$, $\overline{C} = C$, $\overline{U} = U$.

The pressure splitting coefficient is:

$$\mathcal{P}^{\pm}_{L,R} = \frac{1}{4}\left(M_{L,R} \pm 1\right)^2 \left(2 \mp M_L\right) \tag{35}$$

4.2 The Fifth-Order WENO Scheme

The interface flux, $E_{i+\frac{1}{2}} = E(Q_L, Q_R)$, is evaluated by determining the conservative variables Q_L and Q_R using fifth-order WENO scheme[38]. For example,

$$(Q_L)_{i+\frac{1}{2}} = \omega_0 q_0 + \omega_1 q_1 + \omega_2 q_2 \tag{36}$$

where

$$\begin{aligned} q_0 &= \tfrac{1}{3}Q_{i-2} - \tfrac{7}{6}Q_{i-1} + \tfrac{11}{6}Q_i \\ q_1 &= -\tfrac{1}{6}Q_{i-1} + \tfrac{5}{6}Q_i + \tfrac{1}{3}Q_{i+1} \\ q_2 &= \tfrac{1}{3}Q_i + \tfrac{5}{6}Q_{i+1} - \tfrac{1}{6}Q_{i+2} \end{aligned} \tag{37}$$

$$\omega_k = \frac{\alpha_k}{\alpha_0 + \ldots + \alpha_{r-1}} \tag{38}$$

$$\begin{aligned} &\alpha_k = \tfrac{C_k}{\epsilon + IS_k},\ k = 0, \ldots, r-1 \\ &C_0 = 0.1,\ C_1 = 0.6,\ C_2 = 0.3 \\ &IS_0 = \tfrac{13}{12}\left(Q_{i-2} - 2Q_{i-1} + Q_i\right)^2 + \tfrac{1}{4}\left(Q_{i-2} - 4Q_{i-1} + 3Q_i\right)^2 \\ &IS_1 = \tfrac{13}{12}\left(Q_{i-1} - 2Q_i + Q_{i+1}\right)^2 + \tfrac{1}{4}\left(Q_{i-1} - 4Q_i + 3Q_{i+1}\right)^2 \\ &IS_2 = \tfrac{13}{12}\left(Q_i - 2Q_{i+1} + Q_{i+2}\right)^2 + \tfrac{1}{4}\left(Q_i - 4Q_{i+1} + 3Q_{i+2}\right)^2 \end{aligned} \tag{39}$$

where, ϵ is originally introduced to avoid the denominator becoming zero and is supposed to be a very small number. In [38], it is observed that IS_k will oscillate if ϵ is too small and also shift the weights away from the optimum values in the smooth region. The higher the ϵ values, the closer the weights approach the optimum weights, C_k, which will give the symmetric evaluation of the interface flux with minimum numerical dissipation. When there are shocks in the flow field, ϵ can not be too large to maintain the sensitivity to shocks. In [38], $\epsilon = 10^{-2}$ is recommended for transonic flows with shock waves.

The viscous terms are discretized by a fully conservative fourth-order accurate finite central differencing scheme developed by Shen et al.[38, 44].

4.3 Implicit Time Integration

The time dependent governing equations are solved using dual time stepping method suggested by Jameson[45]. To achieve high convergence rate, the implicit pseudo time marching scheme is used with the unfactored Gauss-Seidel line relaxation. The physical temporal term is discretized implicitly using a three point, backward differencing as the following:

$$\frac{\partial \mathbf{Q}}{\partial t} = \frac{\mathbf{3Q^{n+1} - 4Q^{n} + Q^{n-1}}}{2\Delta t} \tag{40}$$

where $n-1$, n and $n+1$ are three sequential time levels, which have a time interval of Δt. The first-order Euler scheme is used to discretize the pseudo temporal term. The semi-discretized equations of the governing equations are finally given as the following:

$$\left[\left(\frac{1}{\Delta\tau} + \frac{1.5}{\Delta t}\right) I - \left(\frac{\partial R}{\partial \mathbf{Q}}\right)^{n+1,m}\right] \delta\mathbf{Q^{n+1,m+1}} = \mathbf{R^{n+1,m}} - \frac{\mathbf{3Q^{n+1,m} - 4Q^{n} + Q^{n-1}}}{\mathbf{2\Delta t}} \tag{41}$$

where the $\Delta\tau$ is the pseudo time step, R is the net flux evaluated on a grid point using the fifth-order WENO scheme and the fourth-order central differencing scheme[38]. Within each physical time step, the L2 norm residual of the RHS is required to be reduced by 4 orders of magnitude.

5 Equations of Motion

The NLR7301 airfoil is elastically mounted as shown in Fig. 1. The non-dimensional form of the equations governing the motion of the two-degree-of-freedom spring/
mass/damper system are:

$$\begin{pmatrix} 1 & -x_\alpha \\ -x_\alpha & r_\alpha^2 \end{pmatrix} \frac{\partial^2 q}{\partial t^2} + 2 \begin{pmatrix} \delta_h \omega_h & 0 \\ 0 & r_\alpha^2 \delta_\alpha \omega_\alpha \end{pmatrix} \frac{\partial q}{\partial t} + \begin{pmatrix} \omega_h^2 & 0 \\ 0 & r_\alpha^2 \omega_\alpha^2 \end{pmatrix} q = \frac{2}{\pi\mu} \begin{pmatrix} c_l \\ c_m \end{pmatrix} \tag{42}$$

where, x_α is the static unbalance, r_α is radius of gyration, ω_α is uncoupled circular pitching frequency, ω_h is uncoupled circular heave frequency, δ_α is Lehr pitching damping, δ_h is Lehr heave damping, μ is mass ratio, c_l and c_m are lift and moment coefficients respectively. q is defined by:

$$q = \begin{pmatrix} q_1 \\ q_2 \end{pmatrix} = \begin{pmatrix} h \\ \alpha - \alpha_0 \end{pmatrix} \tag{43}$$

where h and α are the plunging and pitching displacements respectively, α_0 is the off-wind value of α. The Eqs.(42) are transformed to a state matrix form and expressed as

$$M\frac{\partial S}{\partial t} + K \cdot S = Q \tag{44}$$

where

$$S = \begin{pmatrix} q_1 \\ \frac{\partial q_1}{\partial t} \\ q_2 \\ \frac{\partial q_2}{\partial t} \end{pmatrix}, \ M = \begin{pmatrix} 1 & 0 & 0 & 0 \\ 0 & 1 & 0 & -x_\alpha \\ 0 & 0 & 1 & 0 \\ 0 & -x_\alpha & 0 & r_\alpha^2 \end{pmatrix}, K = \begin{pmatrix} 0 & -1 & 0 & 0 \\ \omega_h^2 & 2\delta_h\omega_h & 0 & 0 \\ 0 & 0 & 0 & -1 \\ 0 & 0 & r_\alpha^2\omega_\alpha^2 & 2r_\alpha^2\delta_\alpha\omega_\alpha \end{pmatrix}, \ Q = \begin{pmatrix} 0 \\ \frac{2}{\pi\mu}c_l \\ 0 \\ \frac{2}{\pi\mu}c_m \end{pmatrix}$$

The structural equations (44) are discretized and solved implicitly in each physical time step in a manner consistent with flow governing equations (1):

$$\left(\frac{1}{\Delta\tau}I + \frac{1.5}{\Delta t}M + K\right)\delta S^{n+1,m+1} = Q^{n+1,m+1} - M\frac{3S^{n+1,m} - 4S^n + S^{n-1}}{2\Delta t} - KS^{n+1,m} \tag{45}$$

The fluid-structural interaction is implemented in a fully couple manner[18, **?**, 19]. Within each physical time step, the flow equations and structural equations are iterated simultaneously until the prescribed convergence criteria are satisfied for both flow and structural solver. After the convergence criteria are reached with the max-Norm residual smaller than 10^{-6}, the fluid-structural interaction goes to next physical time step.

6 Results and Discussion

In this study, the fluid-structural interaction of NLR7301 airfoil is calculated by using RANS with S-A one equation model and DES respectively. The case simulated is the test case No.77[46, 22, 23] of NLR7301 airfoil. The chord length of the airfoil is $0.3m$ and the mean angle of attack is $1.28°$. The experimental conditions are the free-stream Mach number of 0.768 and the Reynolds number of 1.727×10^6 based on the chord length. The experiment was conducted at a total pressure of $p_t = 0.45$ bar and a dynamic pressure of $p_{dyn} = 0.126$ bar.

The nondimensional structural parameters used for the computation of fluid-structural interaction are summarized in table 1

Since there exists always some discrepancy between the experiment and numerical simulation, which may be resulted form the experimental and numerical uncertainties. In addition, it is observed that the LCOs are sensitive to initial conditions. It is difficult to match the numerical initial perturbations with those in experiment. That is, if we directly use the experimental conditions only, the results may not match the experiment well, or could be totally different. The numerical simulation hence involves a search process to match the experimental conditions and results as much as possible.

Mach number	x_α	r_α	δ_α	δ_h	μ	ω_α	ω_h
0.768	0.0484	0.197	0.0041	0.0073	942	0.31988	0.24306
0.753	0.0484	0.197	0.0041	0.0073	942	0.32625	0.24790

Table 1: The nondimensional structural parameters used for computation

In our numerical simulation, it is observed that the factors affecting LCO are Mach number, AoA and α_0. The present study investigates the effects of these factors and search the values that the computed LCO agrees best with the experiment. Two different procedures are conducted to simulate the LCO.

The procedure 1 follows the criterion used by Weber et al.[21] and Tang et al.[1], in which, both Mach number and AoA are adjusted to match steady state surface pressure distribution between computation and experiment as much as possible. The obtained Mach number and AoA are then used in the LCO simulation by adjusting the α_0 until the computed time-averaged AoA is close to the obtained AoA of the steady state computation.

The procedure 2 is developed in this research, in which the Mach number is fixed as the experimental value of 0.768. The α_0 and initial AoA are adjusted until the LCO amplitudes agree with the experiment. The resulted time-averaged lift and moment are also taken into account to compare with the experiment.

All simulations are conducted on an MPI based computer cluster with parallel computation. The parallel computation is performed by a high efficiency algorithm with a general mapping procedure developed for multi-block structured grid CFD methods[47].

6.1 Steady State Flow Computation

The baseline grid is a single block O-type grid with dimensions of 193×97 and is equally partitioned into 16 sub-blocks with 8 blocks in the circumferential direction and two blocks in radial direction as shown in Fig. 2. The dimensions of each sub-block is 25×49.

The steady state computations are conducted first to search for the flow conditions that match the computed pressure distribution best with the experiment. Both the widely used Mach number of 0.753 for CFD[21, 1] and the experimental Mach number of 0.768 are simulated. It is found that the steady state surface pressure agrees best with experiment at $AoA = -0.45^\circ$ for Mach number 0.753 and at $AoA = -0.2^\circ$ for Mach number 0.768. However, neither case agrees with experiment as satisfactory as it is wished. Fig. 3 shows the surface pressure distribution for the two cases. For the case of Mach number 0.753, the shock location at suction surface agrees better with the experiment, whereas for the Mach number 0.768, the shock location at pressure surface agrees better. Overall, the computed case with the experimental Mach number of 0.768 is closer to the experiment upstream and downstream of the shocks.

6.2 2D LCO Simulation Using RANS

6.2.1 $Mach = 0.753$

The first trail uses the procedure 1 at $Mach = 0.753$ and $AoA = -0.45°$, which are the conditions used by the research groups of Weber et al. and Tang et al.[21, 1]. The LCO computation is conducted by adjusting α_0, the off-wind value of α to make the time-averaged AoA agree with $AoA = -0.45°$. The LCO computation is conducted using two different initial flow fields to investigate the effects of initial flow and perturbation. One initial field is the solution of the steady state computation. The other initial field is the uniform free stream. Both LCO computations start at $AoA = 0°$. The dimensionless physical time step of 0.01 is used which is defined as $t_c = t/(c/u_\infty)$. t is the physical time.

The convergence history within a typical physical time step is shown in Fig. 4 at Mach number of 0.753 and α_0 of 0.25°, which shows it takes 14 iterations to reduce the L2 norm residual by 4 orders of magnitude. Fig. 5 and 6 show the computed LCO amplitudes. Both initial fields predict the final LCOs with about the same amplitudes even though the transition period is different. This is different from the conclusion of Tang et al.[1] that the greater initial perturbation has an diminishing effect on the amplitudes of the computed limit cycle. Fig. 7 and 8 plot the lift and moment coefficients respectively.

The second trail uses the procedure 2 at the Mach number 0.753. The LCO is conducted by iterating α_0 and initial AoA to match the measured LCO amplitudes.

Table 2 lists the iteration cases with Mach number 0.753. Case A shows the computed results using procedure 1. Case B to Case F show the computed results with the initial field setup as uniform free stream at the different AoA and α_0 using procedure 2.

It can be seen from table 2 that the Case A matches the moment coefficient best with the experiment. The lift coefficients are under predicted. The predicted LCO amplitudes are an order of magnitude higher than the experiment.

Table 2 indicates that both AoA and α_0 have influence on the amplitudes of LCO. However, the computation is not able to match the amplitudes by adjusting AoA and α_0. The predicted LCO amplitudes for all the cases are an order of magnitude higher than the experiment.

Table 2: Comparison of the test cases at $M = 0.753$

NLR7301 LCO	Initial AoA	α_0°	Lift Coef.	Moment Coef.	$h(mm)$	α°
Case A	0.0	0.25	0.2318	-0.0800	10.134	3.1942
Case B	0.0	0.60	0.2944	-0.0744	9.6768	2.9796
Case C	0.0	0.75	0.3180	-0.0756	8.6943	2.6921
Case D	0.0	0.85	0.3365	-0.0770	7.8386	2.4352
Case E	0.0	0.95	0.3548	-0.0790	6.9359	2.1566
Case F	0.05	0.85	0.3455	-0.0784	7.3517	2.2863
Experiment			0.272	-0.082	0.75	0.20

Fig. 9 shows the contours of Mach number at one cycle for Case E, which has the smallest amplitudes in all the cases at the Mach number 0.753. Fig. 10 and Fig. 11 plot the corresponding positions of (a) to (j) in a cycle for pitching and plunging movement respectively. The phase difference between pitching and plunging movement is 168°. The experimental data is 176°. Under this large amplitude LCO, the shock location and strength vary significantly. At position a), the AoA is maximum. There is only one strong shock on suction surface. With the AoA decreased, the suction surface shock is weakened. At position e), the AoA is the minimum. The double shock pattern is formed on suction surface and the boundary layer on suction surface becomes the thinnest. This is because the shock strength is the weakest with double shock. After position e), the AoA is increased. The shock on suction surface is strengthened with a single shock. The boundary layer on suction surface becomes thick again due to the strong shock/turbulent boundary layer interaction. From position h) to j), while the suction surface shock becomes stronger, the pressure surface shock disappears. As shown in Fig. 12, when the AoA is maximum, there is a small boundary layer separation on the trailing edge.

6.2.2 $Mach = 0.768$

The third trail still uses the procedure 2, but at the experimental Mach number of 0.768. The dimensionless physical time step is the same as the value used in $Mach = 0.753$. The convergence history within a typical physical time step is shown in Fig. 13, which shows that it takes 7 iterations, half of the iterations at Mach 0.753 due to no separation in the flow, to reduce the L2 norm residual by 4 orders of magnitude.

Table 3 lists the iteration cases with Mach number 0.768. It shows that the computed lift and moment coefficients of the final case, Case E, agree excellently with the experiment at initial $AoA = 0.05°$ and $\alpha_0 = 0.75°$. Fig. 14 shows the contours of Mach number at one cycle for case E. Fig. 15 and Fig. 16 plot the corresponding positions of (a) to (j) in a cycle for pitching and plunging movement respectively. The phase difference between pitching and plunging movement is 172°, which is very close to the experimental value of 176°. Different from the LCO computation at Mach number 0.753, no separation is observed in the simulated flow field (see Fig. 17). The reason is the amplitudes of the LCO is only about 3/1000 of the chord and is too small to generate large angle of attack swing and flow separation. This result may indicate that the nonlinearity of LCO is not necessarily from flow separation. The shock turbulent layer interaction even with no flow separation may be sufficient to trigger the nonlinear LCO.

Table 3: Comparison of the test cases at $M = 0.768$

NLR7301 LCO	Initial AoA	α_0°	Lift Coef.	Moment Coef.	$h(mm)$	α°
Case A	0.0	0.68	0.2610	-0.0796	1.6509	0.4632
Case B	0.0	0.70	0.2758	-0.0807	4.2453	1.2349
Case C	0.0	0.75	0.2729	-0.0805	1.2617	0.3524
Case D	-0.033	0.75	0.2673	-0.0799	1.4351	0.4015
Case E	0.05	0.75	0.2803	-0.0816	0.8192	0.2287
Experiment			0.272	-0.082	0.75	0.20

Fig. 18, 19, 20 and 21 show the computed LCO results at Mach number of 0.768 for Case E. Compared with results predicted at $Mach = 0.753$ as shown in Fig. 5, 6, 7 and 8, it can be seen that the predicted amplitudes at $Mach = 0.768$ are more than one order of magnitude smaller. This means that the Mach number has a significant effect on the amplitudes of plunge and pitch modes. The reason may be that the different Mach number causes different shock strength, different shock/boundary layer interaction patterns and hence different unsteady non-linear forcing and moment.

Table 4 shows the computed LCO amplitudes and frequencies compared with the experimental results [22]. At $Mach = 0.753$, the present computed results are comparable with those of Weber et al. and Tang et al. However, at $Mach = 0.768$, which is the experimental condition, both the predicted plunge and pitch amplitudes agrees excellently with the experiment. Using the experimental results as the basis and compared with the results of Weber et al. and Tang et al.[21, 1], the improvement is very significant at 726% to 928% respectively. The computed LCO frequency at $Mach = 0.768$ also agrees very well with the experiment. In general, the prediction accuracy is in the same order of the experiment measurement uncertainty. The only primary difference from the experiment for Case E is that the α_0 used in the simulation is 0.75° whereas the experimental value is 1.28°. The α_0 only affects the initial moment imposed on the elastic system and remains as a constant in the whole LCO process. Such difference may be attributed to the uncertainty of the experiment and numerical simulation, and the sensitive nature of LCO to initial perturbations, which are difficult if not impossible to be made the same between the experiment and numerical simulation.

Table 4: LCO comparison of computation and experiment

NLR7301 LCO	M	$h(mm)$	error%	α°	error	$f(Hz)$	error (Hz)
Present	0.768	0.8192	9.23%	0.2287°	0.0287°	33.15	0.41
Present	0.753	10.134	1251.2%	3.1942°	2.9942°	33.34	0.6
Weber et al. (2001)	0.753	10.5	1300%	4.09°	3.89°	33.42	0.68
Tang et al. (2003)	0.753	8.99	1098.7%	3.17°	2.97°	34.3	1.56
Experiment	0.768	0.75		0.20°		32.74	

Note that the final LCO plunge amplitude is about 2.7/1000 of the chord length and the pitching amplitude is 0.2287°. These are some very small values. The accurate resolution of such small scale vibration motion without being damped out in the long time calculation may have to be attributed to the high order low diffusion numerical schemes, the fully coupled FSI model, and the turbulence model employed and developed in this research.

It needs to point out an important phenomenon that the final LCO amplitudes are dependent on the initial flow fields. The results in Table 4 are computed using the initial field set equal to the uniform free-stream everywhere. If a converged steady state solution is used as the initial field, the final LCO amplitudes may be totally different with significantly greater magnitude. The iterated α_0 and initial AoA also setup the initial lift and moment to certain values. In other words, different initial perturbation may generate very different final LCO solutions. This may be the bifurcation phenomenon due to the non-linear aerodynamic loading of lift and moment, which are caused by the pattern of shock wave/turbulent boundary layer interaction. If we can understand the systematic relationship between the final LCO amplitude and initial perturbation, it may be possible to control the LCO and mitigate or prevent it. For the 2D simulation using 16 processors with the residual reduced at least 4 orders of magnitude within each physical time step, it usually will take 1 to 2 days to complete one LCO simulation.

6.3 3D LCO Simulation Using DES

Based on the results and experience of the 2D LCO simulation using RANS, the 3D DES of LCO for the same condition is conducted. The same structural equations (42)-(44) are used with the same fully coupled fluid-structural interaction procedure. The unsteady lift and moment coefficients are integrated from the 3d unsteady flow fields. The computation grid is composed of 24 blocks partitioned from a single block O-H-grid with the dimension of 193 × 97 × 33 (see Fig. 22). This simulation is very CPU intensive and will be impossible without parallel computation. The span wise length is 3.33, which is the same as the experiment. The dimensionless physical time interval is 0.01. The second procedure is employed in 3D LCO simulation. Based on the experience of 2D LCO simulation, the computation is implemented with experimental Mach number 0.768 only. Three cases are performed with the different initial AoA and α_0.

Case A: $AoA = 0.05^\circ$**,** $\alpha_0 = 0.75^\circ$

This case uses the same conditions as the 2D Case E at $Mach = 0.768$. The predicted amplitudes of plunge and pitch modes are shown in Fig. 23 and Fig. 24. Different from the corresponding 2D case, the amplitudes of the 3D case are 4 times higher than the experiment. Fig. 25 and Fig. 26 plot the variation of lift and moment coefficients with the time after the LCO formed. As indicted in table 5, the predicted time-averaged lift coefficient is greater than that of 2D case. The predicted time-averaged moment coefficient is lower than that of 2D case.

Case B: $AoA = 0^\circ$**,** $\alpha_0 = 0.75^\circ$

In this case, the initial AoA is decreased to zero to observe the variation of the LCO. The predicted amplitudes of plunge and pitch modes are shown in Fig. 27 and Fig. 28. Fig. 29 and Fig. 30 plot the variation of lift and moment coefficients with the time after the LCO is formed. As shown in table 5, the amplitudes of the LCO are larger than those of case A. Compared with case A, the predicted time-averaged lift coefficient is decreased, on the contrary, the predicted time-averaged moment coefficient is increased.

Case C: $AoA = 0^\circ$**,** $\alpha_0 = 0.85^\circ$

In this case, the α_0 is increased to 0.85°, which is closer to the experimental data 1.28°. The initial AoA is kept the same as the case B. The predicted amplitudes of plunge and pitch modes are shown in Fig. 31 and Fig. 32. Fig. 33 and Fig. 34 plot the variation of lift and moment coefficients with the time after the LCO is formed. As shown in table 5, the amplitudes of the LCO are significantly decreased compared with case A and case B. They are much closer to the experiment than case A and case B. The predicted time-averaged lift coefficient is larger than case A. Both the predicted time-averaged moment and lift coefficients have absolute values a little greater than those of the experiment.

The instantaneous vorticity contours at the left most, right most and middle plane are shown in Fig. 35 at the instant the time dependent AoA reaches its maximum. The DES captures some small vortex structures of the shock/turbulent boundary layer interaction. Table 5 indicates that the Case C is already very close to the experiment even though not as close as the 2D Case E. The search is still in progress and the final result will be reported soon. The 3D DES simulation of LCO is much

Table 5: Comparison of LCO for different initial AoA and α_0 at $M = 0.768$ using DES

NLR7301 LCO	h (mm)	$\alpha°$	Lift Coef.	Moment Coef.
Case A	2.8424	0.8066	0.2934	-0.0831
Case B	3.4313	0.9871	0.2780	-0.0788
Case C	1.0776	0.2920	0.3044	-0.0850
Experiment	0.75	0.20	0.272	-0.082

more CPU intensive than the 2D simulation. With 24 CPU processors and the L2 norm residual reduced by 4 orders of magnitude within each physical time step, it will take about 30-45 days to complete a LCO simulation.

7 Conclusions

A fully coupled fluid-structural interaction is conducted to simulate the nonlinear transonic LCO of NLR7301 airfoil. Both RANS and DES method with a low diffusion E-CUSP scheme [39] and fifth-order WENO scheme are performed in the LCO computation. A fully conservative fourth-order central differencing scheme is used for the viscous terms.

At experimental Mach number of 0.768, the computed LCO amplitudes are in excellent agreement with experiment by adjusting AoA and α_0. The time averaged lift and moment coefficients also match the experiment very well. The free-stream Mach number has the major effect on the amplitudes of LCO due to different shock/boundary layer interaction patterns. The initial flow field or initial perturbation has a strong influence on the amplitudes of LCO. In general, the prediction accuracy is in the same order of the experiment measurement uncertainty. The only primary difference from the experiment is that the α_0 used in the simulation is $0.75°$ whereas the experimental value is $1.28°$. The α_0 only affects the initial moment imposed on the elastic system and remains as a constant in the whole LCO process. Such difference may be attributed to the uncertainty of the experiment and numerical simulation, and the sensitive nature of LCO to initial perturbations, which are difficult if not impossible to be made the same between the experiment and numerical simulation. This research appears to be the first time that a numerical simulation of NLR7301 airfoil LCO matches the experiment. It may be attributed to the high order low diffusion numerical schemes, the fully coupled FSI model, and the turbulence model used in this research.

The simulations of this paper also confirm some of the experimental observations and answers some important questions. First, The LCOs with the small relative amplitude is captured with unbounded flows in the numerical simulation. This means they should not be the artefacts of the wind-tunnel experiment and most likely are the factual phenomenon. Second, the co-existence of multiple LCOs at constant flow conditions is confirmed in our simulation. The reason that other numerical simulations only capture the LCOs with large amplitudes may be due to their high numerical dissipation that either smears out the small amplitude LCO or is only able to resolve the large amplitudes LCOs. Third, the numerical simulation of this research confirms that the wall boundary layer transition from laminar to turbulent does not have a large effect on LCOs at high Reynolds number because our simulation assumes that the boundary layer is fully turbulent from the airfoil leading edge. Fourth, the simulation confirms that the wind tunnel wall interference with or without perforated test section does not have much effect on LCOs because the simulation uses the unbounded flow condition with no wind tunnel wall effect at all. Fifth, the numerically captured LCO is not accompanied with any flow separation due to the very small amplitude. This may modify the hypothesis that the LCOs are caused by the nonlinearity of flow separation induced by shock/boundary layer interaction. In other words, the nonlinearity of shock/boundary layer interaction with no flow separation is sufficient to trigger a LCO. This may make reduced numerical models feasible to capture LCOs.

The search of the LCO using 3D DES simulation is approaching the experiment as shown in this paper. The LCO flow behavior of the 3D DES is basically the same as that of the 2D RANS cases since no flow separation occurs. Due to the extensive CPU requirement, the final LCO searched by DES is still in progress and will be reported soon in future.

8 Acknowledgment

This work is supported by AFOSR Grant FA9550-06-1-0198 monitored by Fariba Fahroo.

References

[1] D. M. Tang, H. Yamamoto, and E. Dowell, “Flutter and limit cycle oscillations of two-dimensional panels in three-dimensional axial flow,” *Journal of Fluid and Structures*, vol. 17, 2003.

[2] O. Bendiksen, “Role of Shock Dynamics in Transonic Flutter.” AIAA Paper 92-2121.

[3] O. Bendiksen and K. Kousen, “Transonic Flutter Analysis Using the Euler Equations.” AIAA Paper 87-0911, 1987.

[4] G. Guruswamy, “Unsteady Aerodynamic and Aeroelastic Calculations for Wngs Using Euler Equations,” *AIAA Journal*, vol. 28, pp. 461–469, March 1990.

[5] E. Lee-Rausch and J. Batina, “Wing Flutter Computations Using an Aerodynamics Model Based on the Navier-Stokes Equations,” *Journal of Aircraft*, vol. 33, pp. 1139–1147.

[6] M. Smith, “Flight Loads Prediction Methods for Aircraft: Vol I. Euler/Navier-Stokes Aeroelastic Method (ENS3DAE) Technical Development Summary: Version 4.0.” WRDC-TR-89-3104, 1989.

[7] S. Vermeersch, P. Raj, R. Weed, and L. Sankar, “Towards Cost-Effective Aeroelastic Analysis on Advanced Parallel Computing Systems .” AIAA Paper 97-0646, 1997.

[8] S. Darracq, S. Champagneux, and A. Corjon, “Computation of Unsteady Turbulent Airfoil Flows with an Aeroelastic AUSM+ Implicit Solver.” AIAA Paper-98-2411, 1998.

[9] B. B. Prananta, H. M. H. L., and Z. R. J., “Two-Dimensional Transonic Aeroelastic Analysis Using Thin-Layer Navier-Stokes Method,” *Journal of Fluid and Structures*, vol. 12, pp. 655–676, 1998.

[10] J. Bohbot and D. Darracq, “Time Domain Analysis of Two D.O.F. Airfoil Flutter Using an Euler/Turbulent Navier-Stokes Implicit Solver.” International Forum on Aeroelasticity and Structural Dynamics, Madrid, Spain, June 5-7, 2001.

[11] F. J. Blom and P. Leyland, “Analysis of Fluid-Structure Interaction by Means of Dynamic Unstructured Meshes.” AD-Vol. 53-3, 4th International Symposium on Fluid-Structure Interaction, Aeroelasticity, Flow-Induced Vibrations and Noise, Volume I, ASME, 1997.

[12] J. J. Alonso and A. Jameson, “Fully-Implicit Time-Marching Aeroelastic Solutions.” AIAA Paper 94-0056, 1994.

[13] J. Alonso, L. Martinelli, and A. Jameson, “Multigrid Unsteady Navier-Stokes Calculations with Aeroelastic Applications.” AIAA Paper 95-0048, 1995.

[14] S. A. Morton, R. B. Melville, and M. R. Visbal, “Accuracy and Coupling Issues of Aeroelastic Navier-Stokes Solutions on Deforming Meshes.” AIAA Paper-97-1085, 1997.

[15] R. B. Melville, S. A. Morton, and D. P. Rizzetta, “Implementation of a Fully-Implicit, Aeroelastic Navier-Stokes Solver.” AIAA Paper-97-2039, 1997.

[16] R. B. Melville and S. A. Morton, “Fully Implicit Aeroelasticity on Oveerset Grid Systems .” AIAA Paper-98-0521, 1998.

[17] F. Liu, J. Cai, Y. Zhu, A. Wong, and H. Tsai, “Calculation of Wing Flutter by a Coupled CFD-CSD Method,” *Journal of Aircraft*, vol. 38, 2001.

[18] X.-Y. Chen, G.-C. Zha, and Z.-J. Hu, “Numerical Simulation of Flow Induced Vibration Based on Fully Coupled-Structural Interactions.” AIAA Paper 2004-2240, AIAA 34th AIAA Fluid Dynamics Conference,, Jaun 28 - July 1, 2004.

[19] X.-Y. Chen, G.-C. Zha, and M.-T. Yang, “Numerical Simulation of 3-D Wing Flutter with Fully Coupled Fluid-Structural Interaction,” *Journal of Computers & Fluids*, vol. 36, No. 5, pp. 856–867, 2007.

[20] S. Morton and P. S. Beran, “Hopf-bifurcation analysis of airfoil flutter at transonic speeds,” *Journal of Aircraft*, vol. 36, 1999.

[21] S. Weber, K. D. Jones, and M. F. Ekaterinaris, J. A.and Platzer, “Transonic flutter computations for the NLR 7301 supercritical airfoil,” *Aerospace Science and Technology*, vol. 5, 2001.

[22] G. Schewe and G. Hai, H.and Dietz, “Nonlinear effects in transonic flutter with emphasis on manifestations of limit cycle oscillation,” *Journal of Fluid and Structures*, vol. 18, 2003.

[23] G. Dietz, G. Schewe, and H. Hai, “Experiments on heave/pitch limit-cycle oscillations of a supercritical airfoil close to the transonic dip,” *Journal of Fluid and Structures*, vol. 19, 2004.

[24] R. E. Gordnier, “Computation of limit-cycle oscillations of a delta wing,” *Journal of Aircraft*, vol. 40, 2003.

[25] B. Castro, J. A. Ekaterinaris, and M. F. Platzer, “Analysis of the effect of propous wall interference on transonic airfoil flutter.” AIAA Paper 2001-2725.

[26] P. Spalart, W.-H. Jou, M. Strelets, and S. Allmaras, “Comments on the Feasibility of LES for Wings, and on a Hybrid RANS/LES Approach.” Advances in DNS/LES, 1st AFOSR Int. Conf. on DNS/LES, Greyden Press, Columbus, H., Aug. 4-8, 1997.

[27] P. R. Spalart, "Young-Person's Guide to Detached-Eddy Simulation Grids." NASA/CR-2001-211032, 2001.

[28] P. R. Spalart, "Topics in Detached-Eddy Simulation."

[29] A. Tarvin, M. Shur, M. Strelets, and P. Spalart, "Detached-Eddy Simulations Past a Circular Cylinder," *Flow Turbulence and Combustion*, vol. 63, 1999.

[30] J. R. Forsythe, K. A. Hoffmann, and K. D. Cummings, R. M. Squires, "Detached-Eddy Simulations with Compressibility Corrections Applied to Supersonic Axisymmetric Base Flow," *Journal of Fluids Engineering*, vol. 124, 2002.

[31] A. Viswanathan, K. Klismith, J. Forsythe, and K. D. Squires, "Detached-Eddy Simulation around a Forebody at High Angle of Attack." AIAA-2003-0263, 2003.

[32] K. D. Squires, "Detached-Eddy Simulation: Current Status and Perspectives."

[33] K. D. Squires, J. R. Forsythe, and P. R. Spalart, "Detached-Eddy Simulation of the Seperated Flow Around a Forebody Cross-Section."

[34] R. P. Hansen and J. R. Forsythe, "Large and Detached Eddy Simulation of a Circular Cylinder Using Unstructured Grids." AIAA Paper 2003-0775, Jan. 2003.

[35] P. Subbareddy and G. V. Candler, "Numerical Investigations of Supersonic Base Flows Using DES." AIAA Paper 2005-0886, Jan. 2005.

[36] B. Wang and G. - C. Zha , " Detached Eddy Simulations of a Circular Cylinder Using a Low Diffusion E-CUSP and High-Order WENO Scheme." AIAA Paper 2008-3855, AIAA 38th Fluid Dynamics Conference, Seattle, Washington, June 23-26, 2008.

[37] C.-W. Shu, "Essentially Non-Oscillatory and Weighted Essentially Schemesfor Hyperbolic Conservation Laws." NASA/CR-97-206253, 1997.

[38] Y.-Q. Shen, B.-Y. Wang, and G.-C. Zha, "Implicit WENO Scheme and High Order Viscous Formulas for Compressible Flows ." AIAA Paper 2007-4431, 2007.

[39] G.-C. Zha, Y. Shen, and B. Wang, "Calculation of Transonic Flows Using WENO Method with a Low Diffusion E-CUSP Upwind Scheme." AIAA Paper 2008-0745, 46th AIAA Aerospace Sciences Meeting, Reno, NV, Jan. 2008.

[40] B. Wang and G.-C. Zha, "Comparison of a Low Diffusion E-CUSP and the Roe Scheme for RANS Calculation." AIAA Paper 2008-0596, 46th AIAA Aerospace Sciences Meeting and Exhibit, Jan. 7-10, 2008.

[41] P. Spalart and S. Allmaras, "A One-equation Turbulence Model for Aerodynamic Flows." AIAA-92-0439, 1992.

[42] R. P. Hansen and J. Forsythe, "Large and Detached Eddy Simulation of a Circular Cylinder Using Unstructured Grids." AIAA-2003-0775, 2003.

[43] M. Shur, P. Spalart, M. Strelets, and A. Travin, "Detached-Eddy Simulation of an Airfoil at High Angle of Attack", 4th Int. Symp. Eng. Turb. Modelling and Measurements, Corsica." May 24-26, 1999.

[44] Y.-Q. Shen, G.-C. Zha, and X. Chen, "Simulation of Fully Coupled Vortex-Induced-Vibration of a Circular Cylinder by Using High Order WENO Scheme." Submitted to 46th AIAA Aerospace Sciences Meeting, Jan. 2008.

[45] A. Jameson, "Time Dependent Calculations Using Multigrid with Application to Unsteady Flows past Airfoils and Wings." AIAA Paper 91-1596, 1991.

[46] A. Knipfer, G. Schewe, and V. Wendt, "Numerische und experimentelle Untersuchungen an einem schwingenden NLR 7301-Profil in transsonischer Stromung." Teil 1: Flatern und erzwungene Schwingungen, DLR Bericht IB 232-98 J 05, 1998.

[47] B.-Y. Wang and G.-C. Zha, "A General Sub-Domain Boundary Mapping Procedure For Structured Grid CFD Parallel Computation," *AIAA Paper 2007-4432, To Appear in AIAA Journal of Aerospace Computing, Information, and Communication*, 2008.

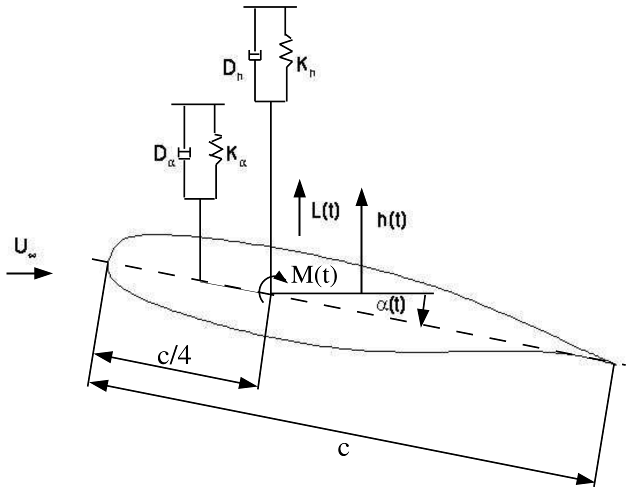

Figure 1: Model of the structural dynamics

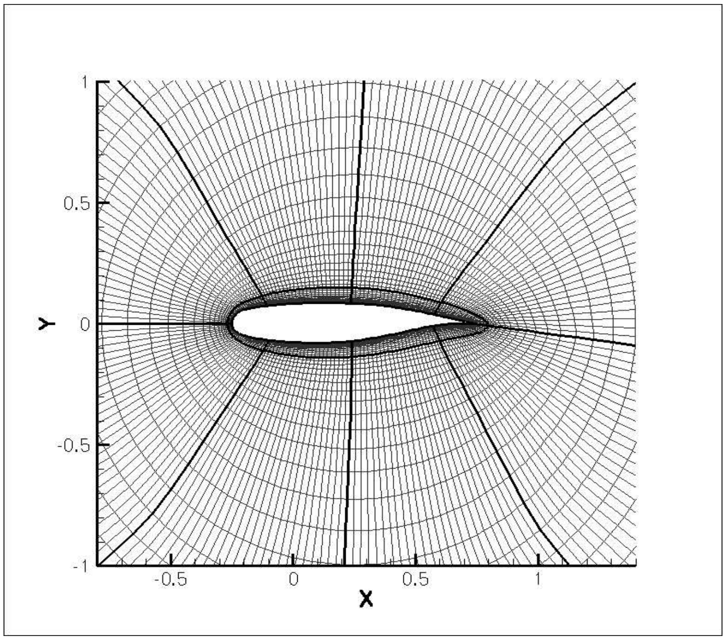

Figure 2: The grid of NLR7301 airfoil

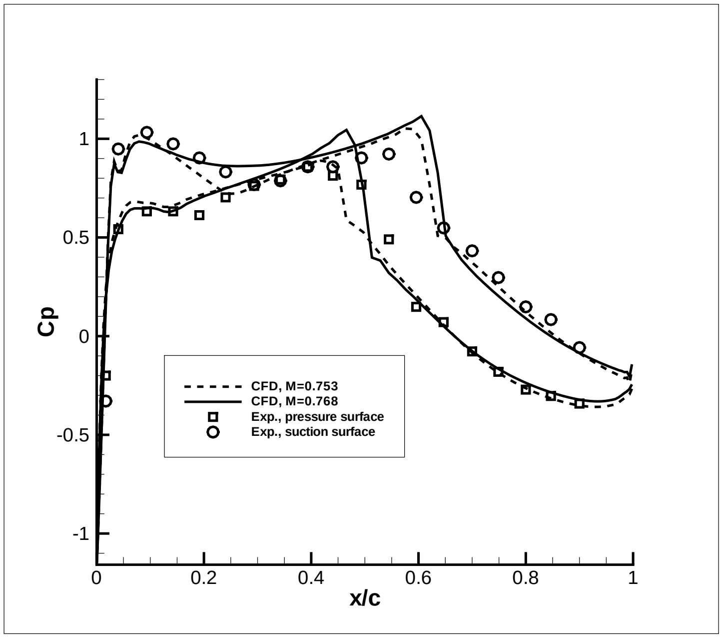

Figure 3: Pressure coefficient distribution on the surface of NLR7301 airfoil

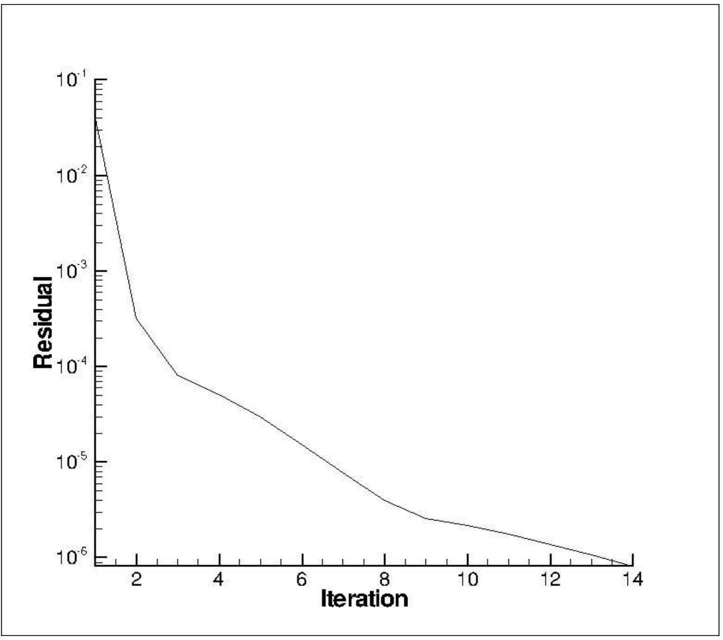

Figure 4: Convergence history within a typical physical time step for $M = 0.753$

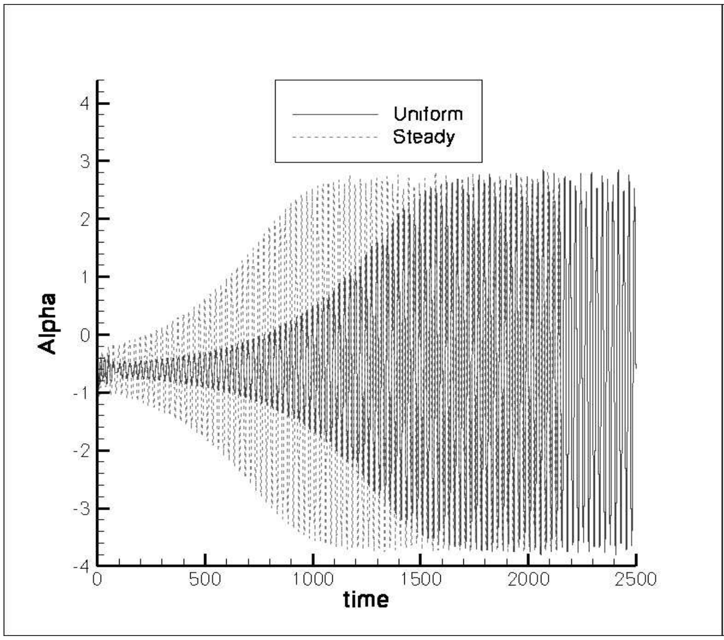

Figure 5: Pitch motion predicted by RANS ($M = 0.753, AoA = -0.45°$)

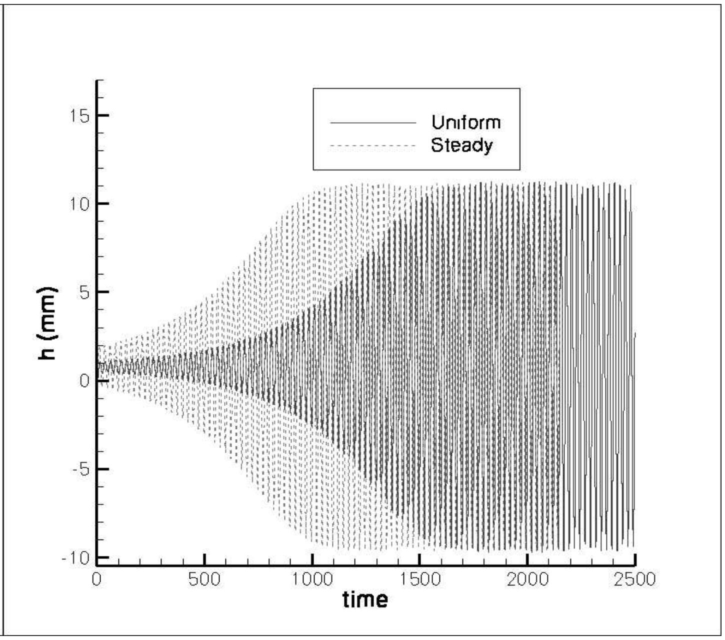

Figure 6: Plunge motion predicted by RANS ($M = 0.753, AoA = -0.45°$)

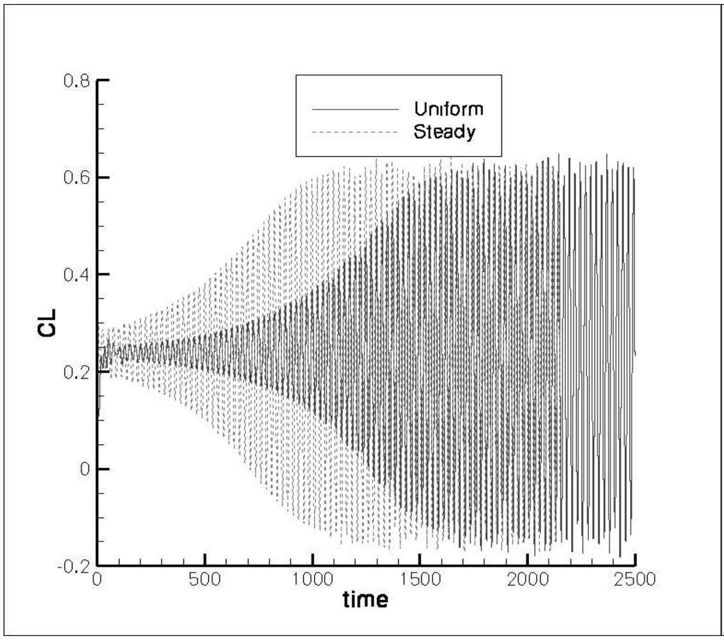

Figure 7: Lift coefficient predicted by RANS ($M = 0.753, AoA = -0.45°$)

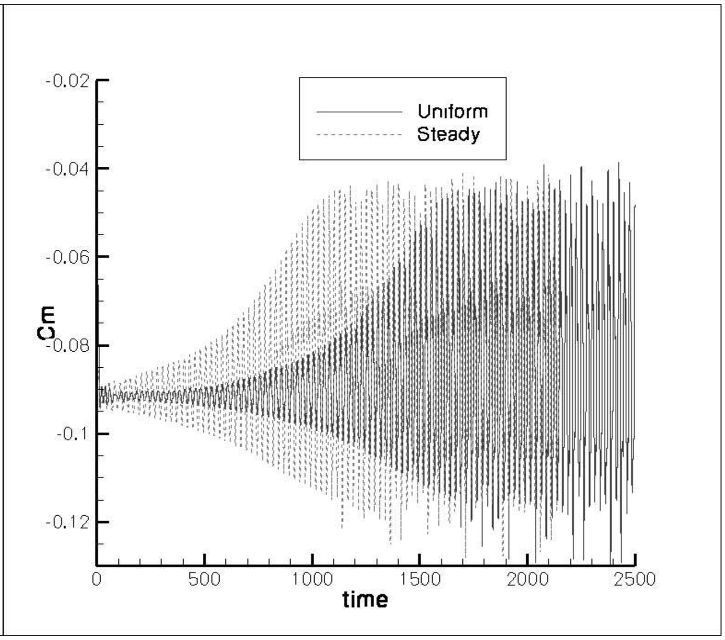

Figure 8: Moment coefficient predicted by RANS ($M = 0.753, AoA = -0.45°$)

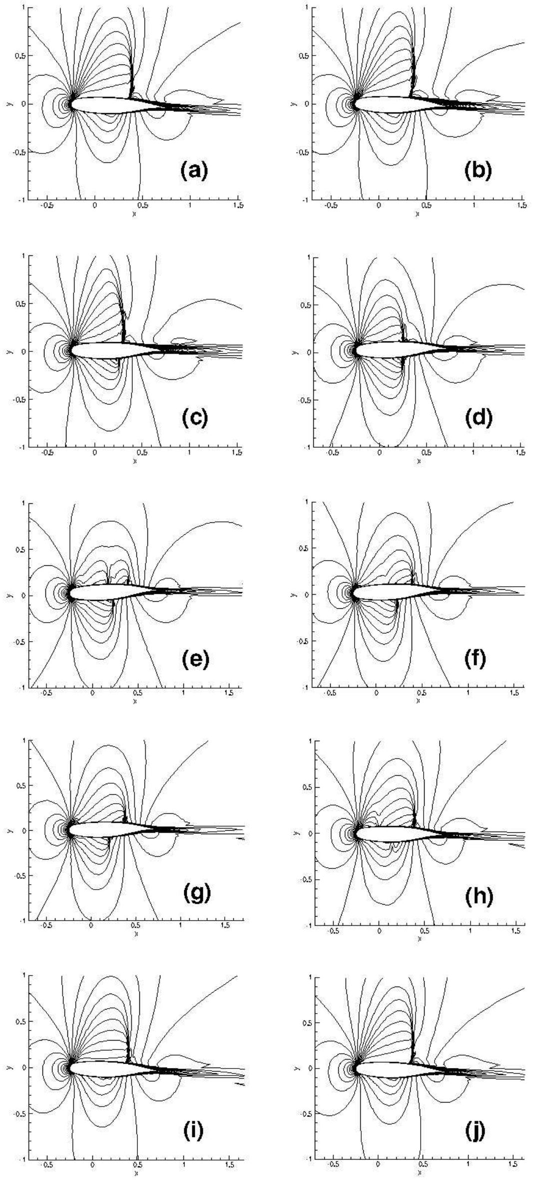

Figure 9: Contours of Mach number for $M = 0.753, AoA = 0°, \alpha_0 = 0.95°$

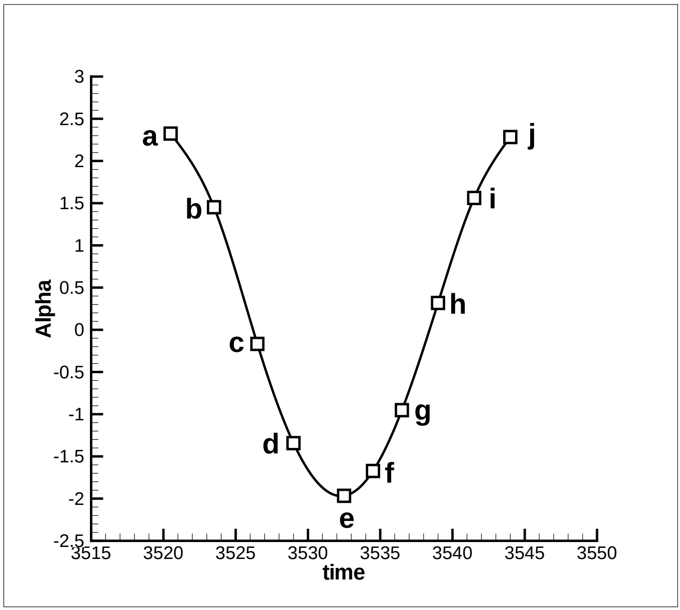

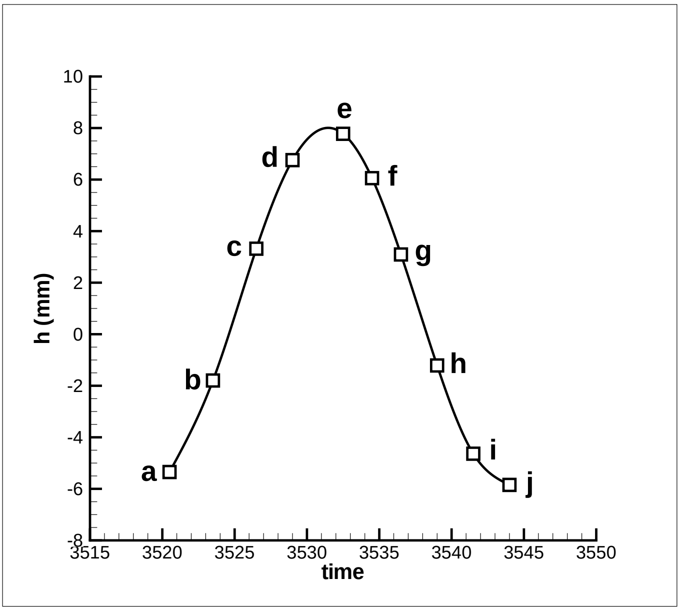

Figure 10: Positions of pitching movement in Fig. 9

Figure 11: Positions of plunging movement in Fig. 9

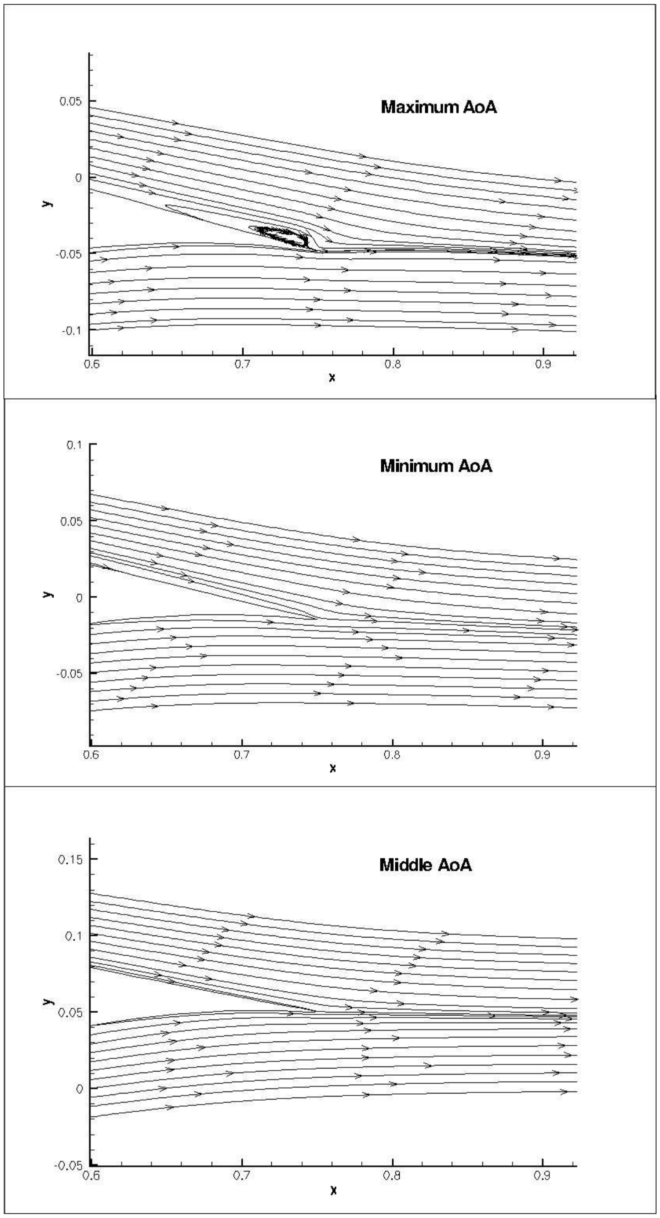

Figure 12: Stream line for Case E at $M = 0.753$

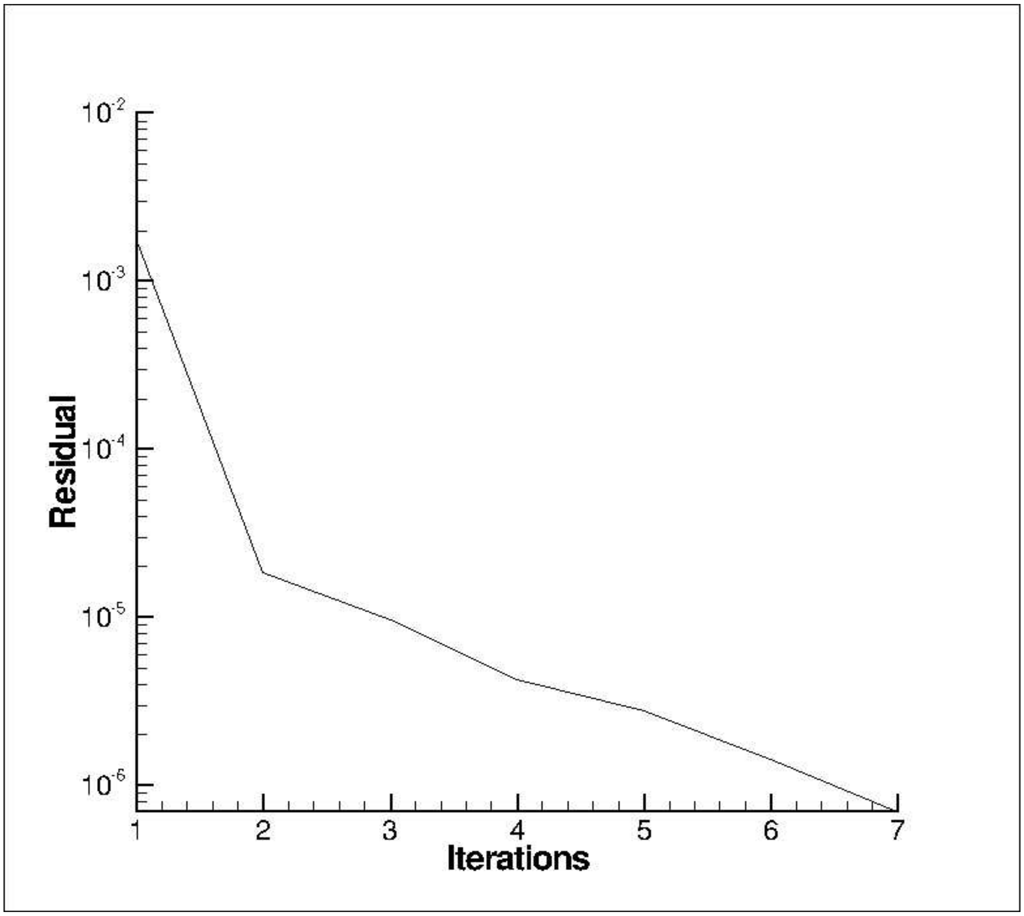

Figure 13: Convergence history within a typical physical time step for $M = 0.768$

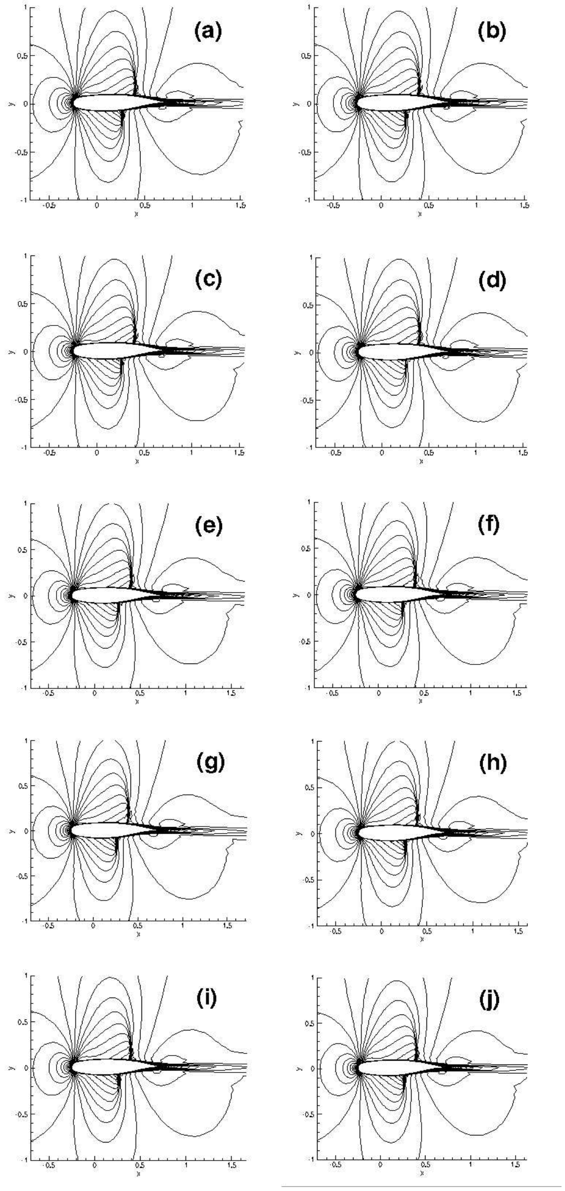

Figure 14: Contours of Mach number for $Mach = 0.768$

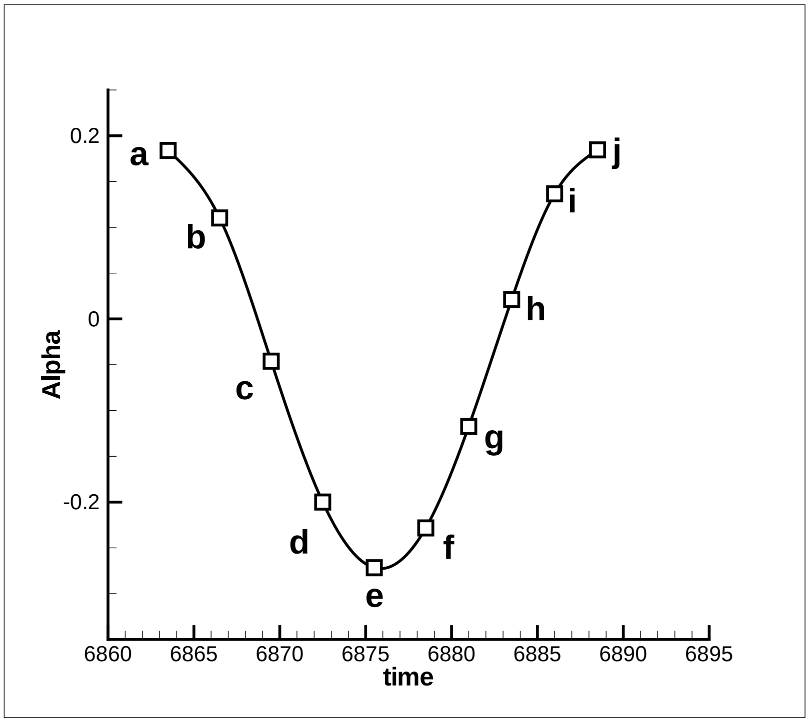

Figure 15: Positions of pitching movement in Fig. 14

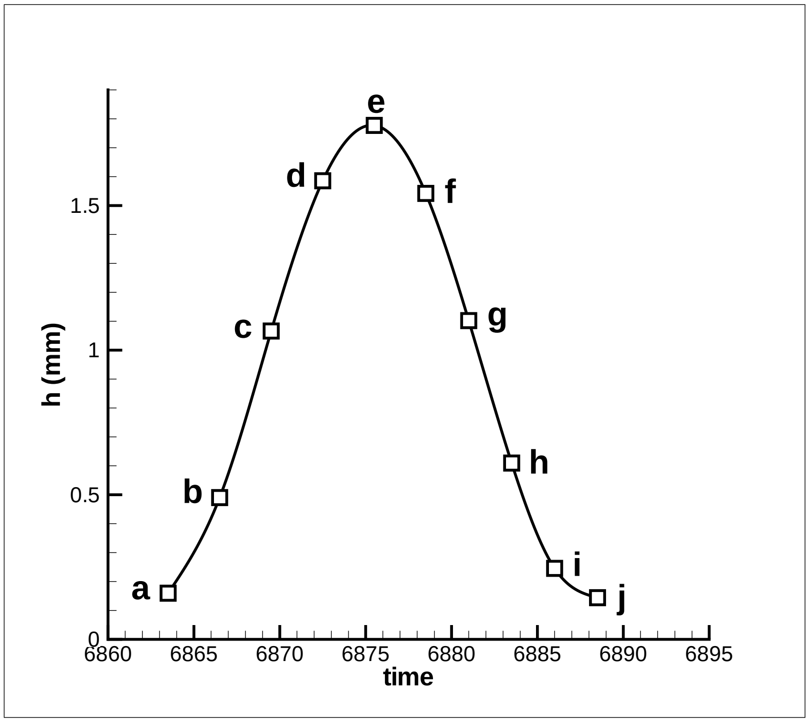

Figure 16: Positions of plunging movement in Fig. 14

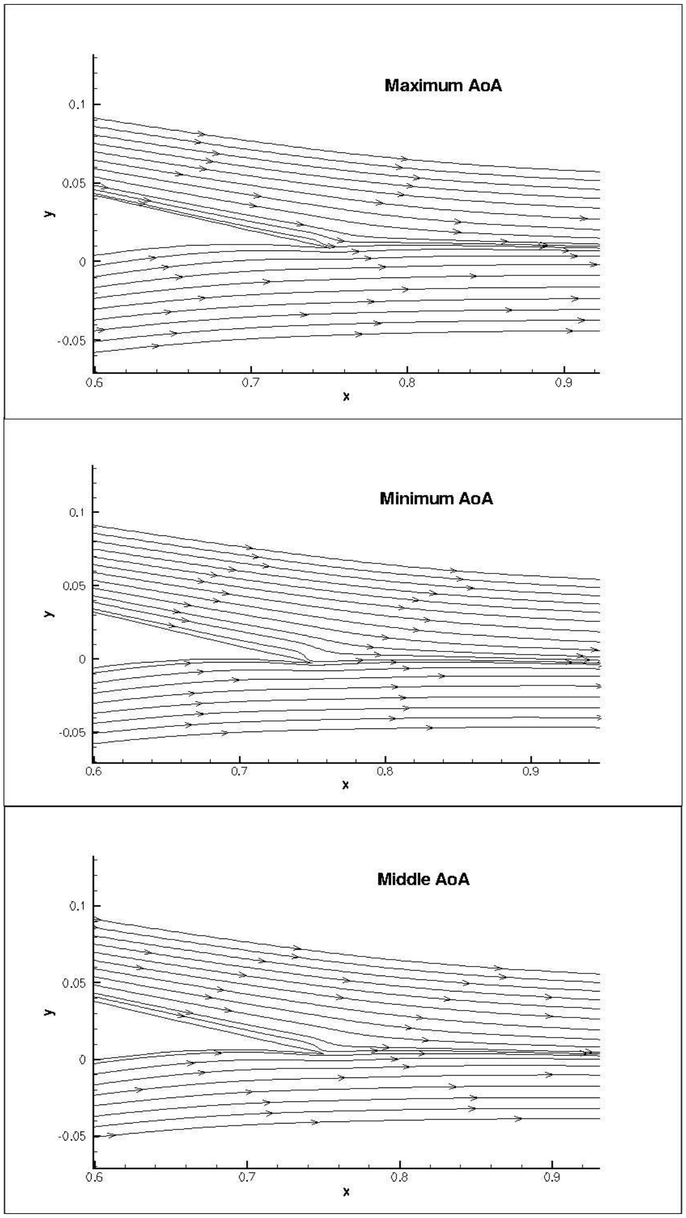
Maximum AoA

Minimum AoA

Middle AoA

Figure 17: Stream line for Case E at $M = 0.768$

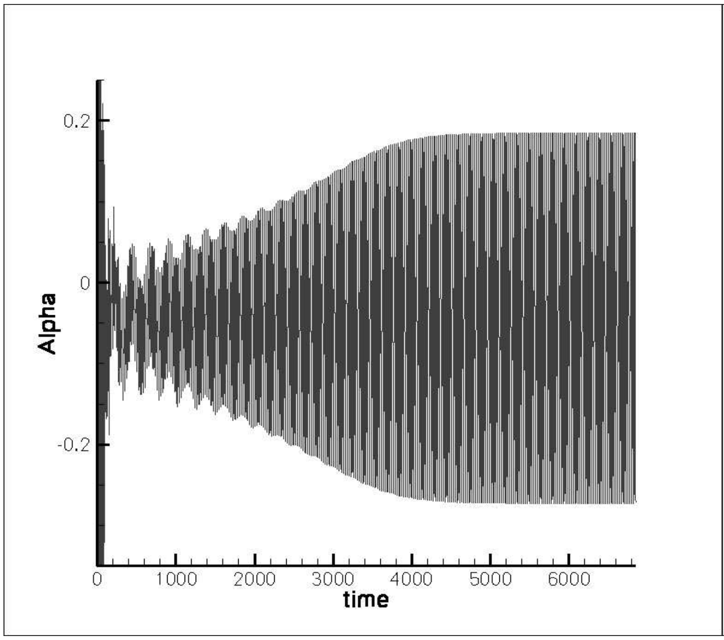

Figure 18: Pitch motion predicted by RANS ($M = 0.768$)

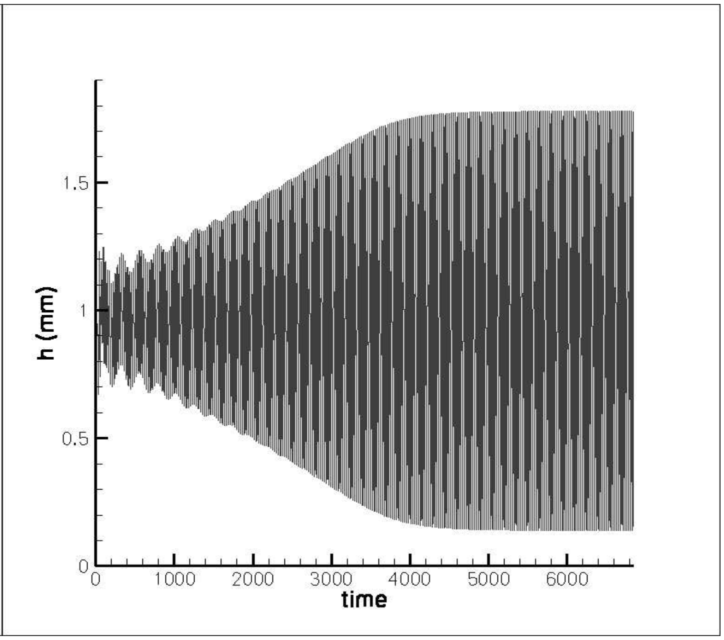

Figure 19: Plunge motion predicted by RANS ($M = 0.768$)

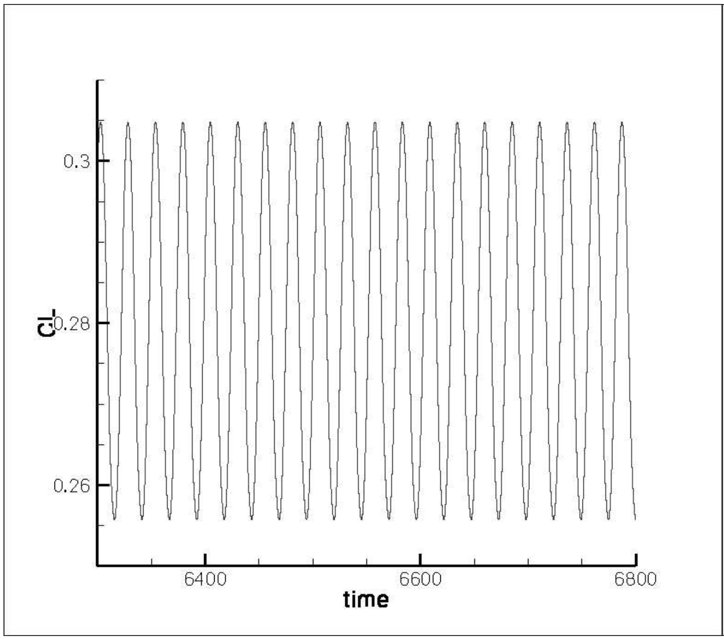

Figure 20: Lift coefficient predicted by RANS ($M = 0.768$)

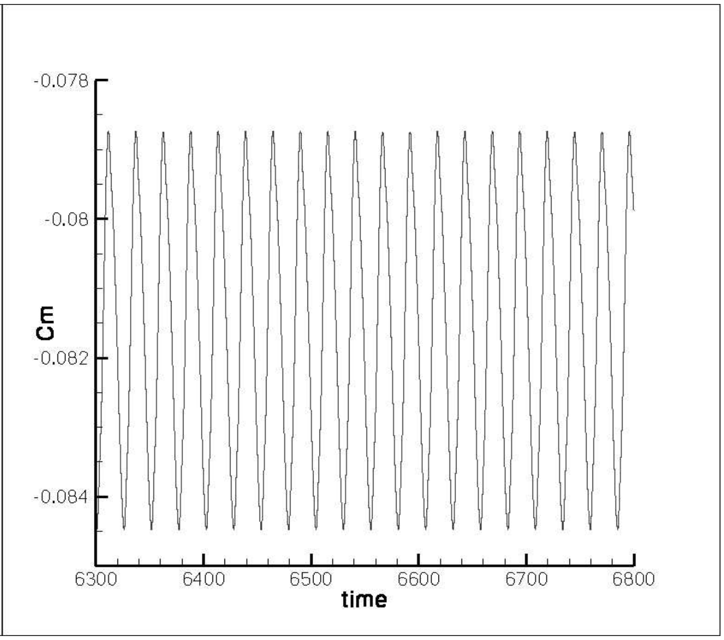

Figure 21: Moment coefficient predicted by RANS ($M = 0.768$)

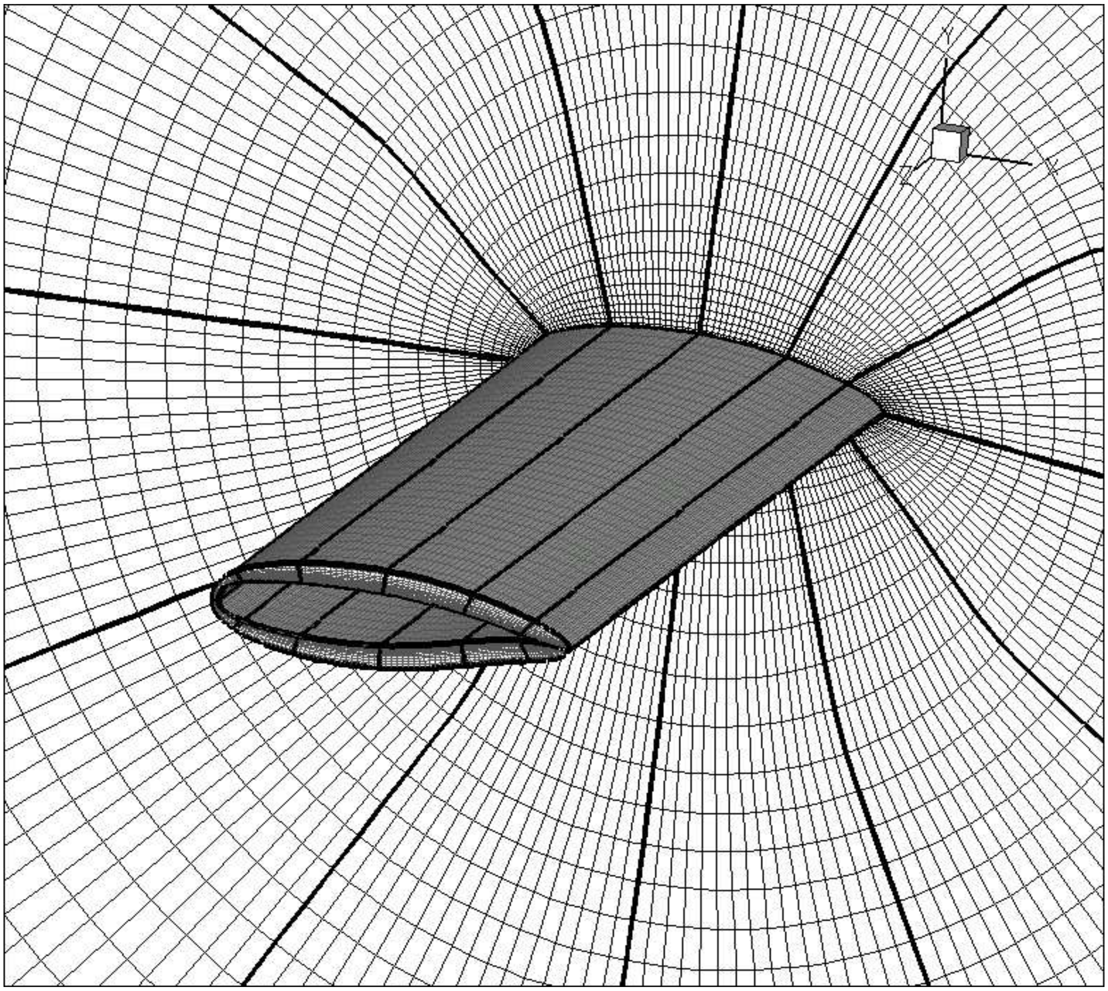

Figure 22: The 3D computational grid of NLR7301 airfoil

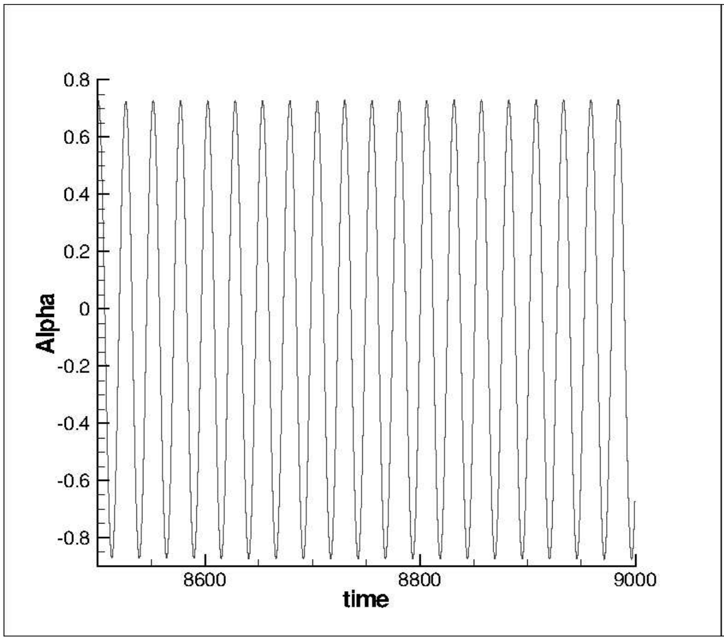

Figure 23: Pitch motion predicted by DES ($AoA = 0.05°, \alpha_0 = 0.75°$)

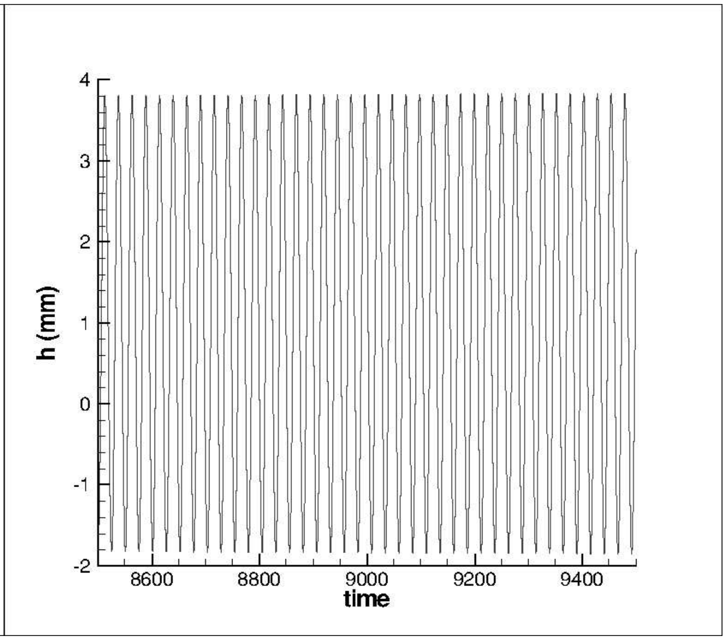

Figure 24: Plunge motion predicted by DES ($AoA = 0.05°, \alpha_0 = 0.75°$)

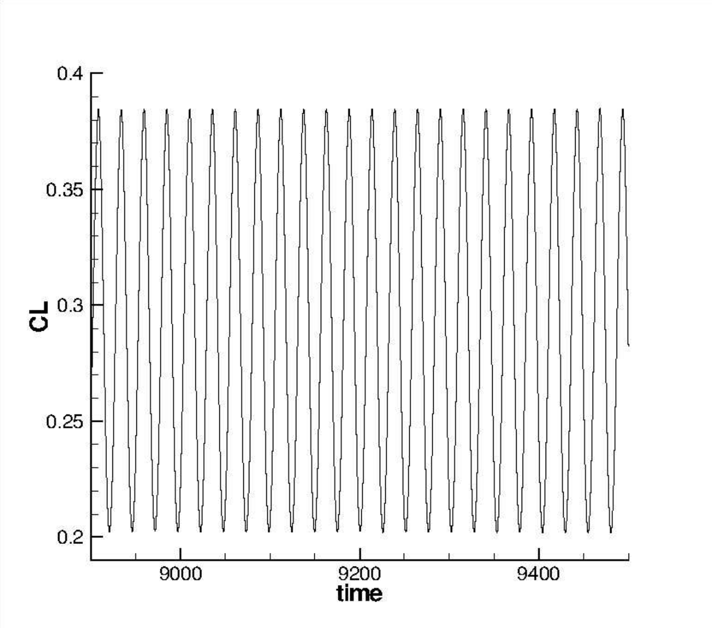

Figure 25: Lift coefficient predicted by DES ($AoA = 0.05°, \alpha_0 = 0.75°$)

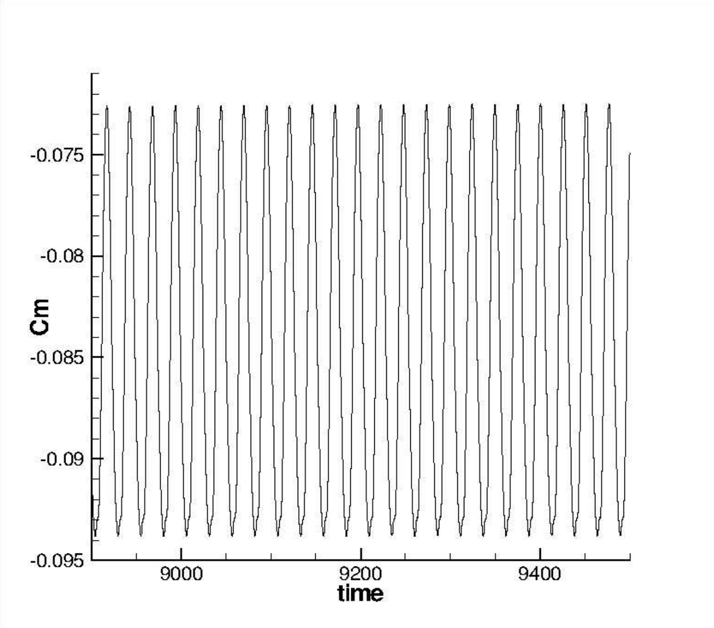

Figure 26: Moment coefficient predicted by DES ($AoA = 0.05°, \alpha_0 = 0.75°$)

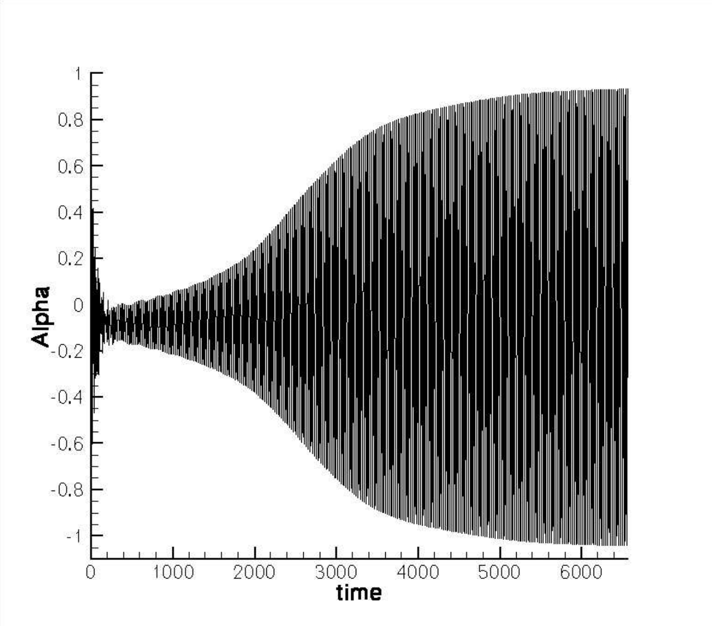

Figure 27: Pitch motion predicted by DES ($AoA = 0.0°, \alpha_0 = 0.75°$)

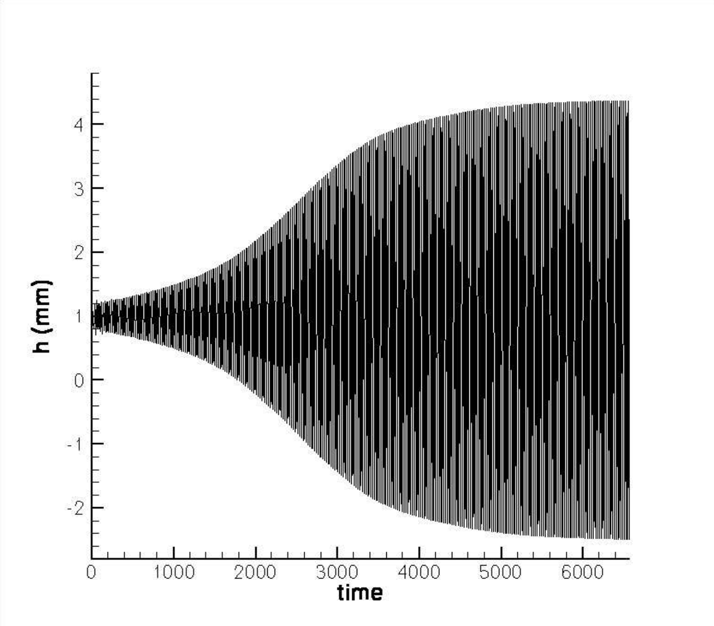

Figure 28: Plunge motion predicted by DES ($AoA = 0.0°, \alpha_0 = 0.75°$)

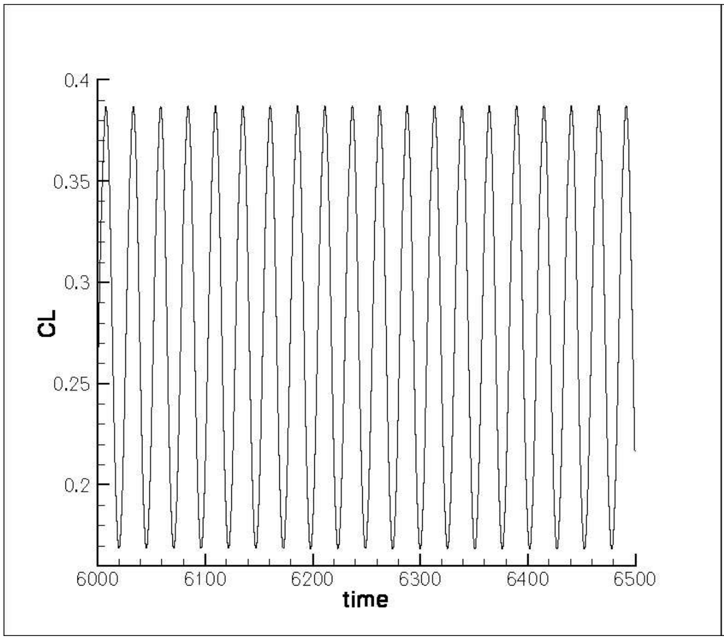

Figure 29: Lift coefficient predicted by DES ($AoA = 0.0°, \alpha_0 = 0.75°$)

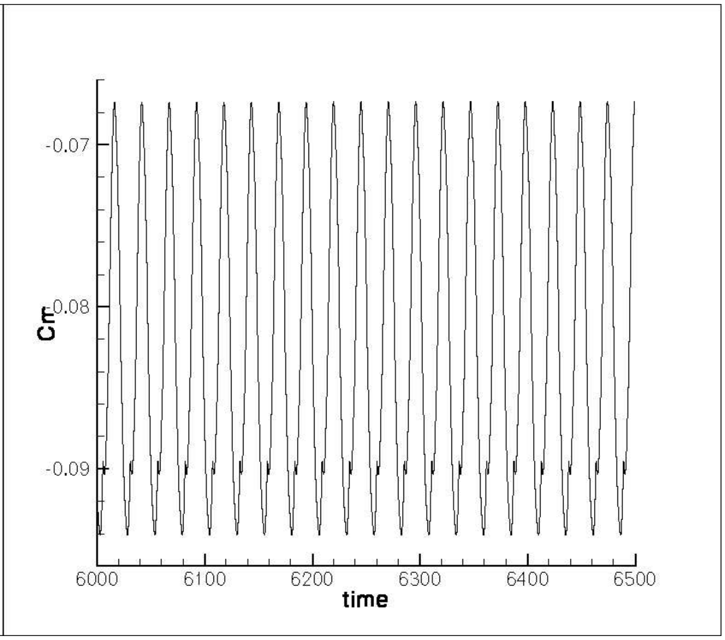

Figure 30: Moment coefficient predicted by DES ($AoA = 0.0°, \alpha_0 = 0.75°$)

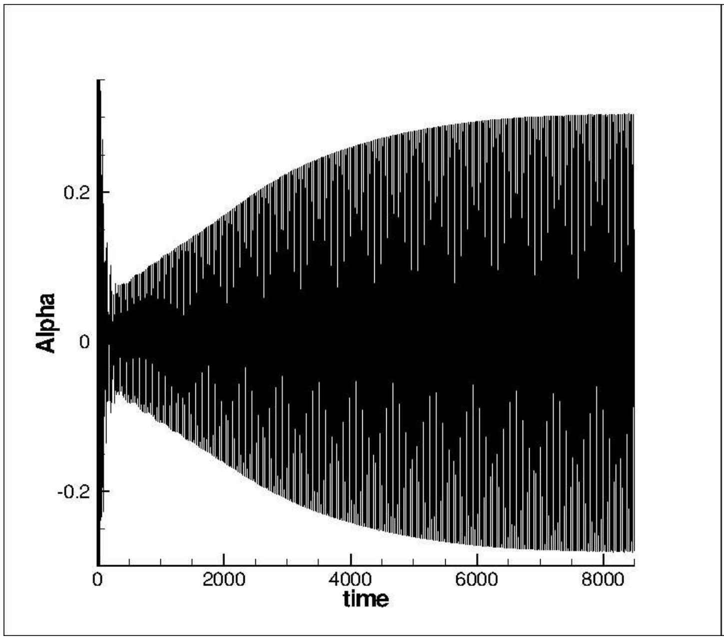

Figure 31: Pitch motion predicted by DES ($AoA = 0.0°, \alpha_0 = 0.85°$)

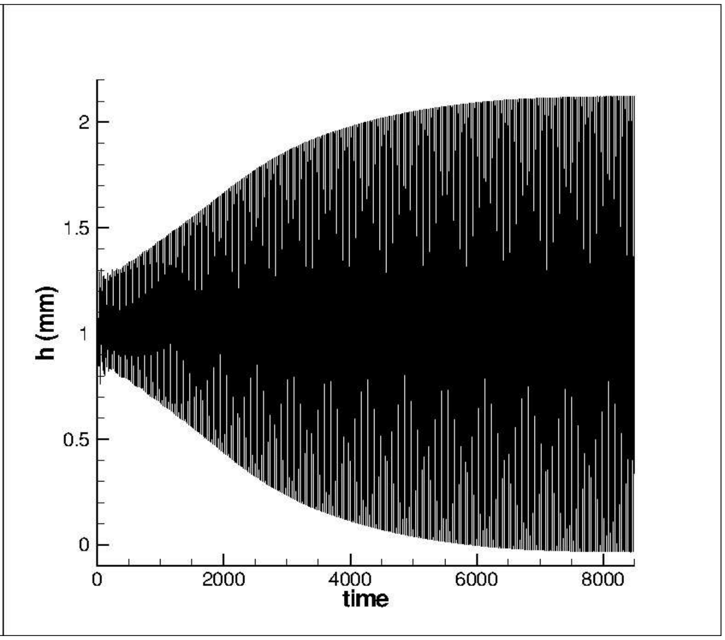

Figure 32: Plunge motion predicted by DES ($AoA = 0.0°, \alpha_0 = 0.85°$)

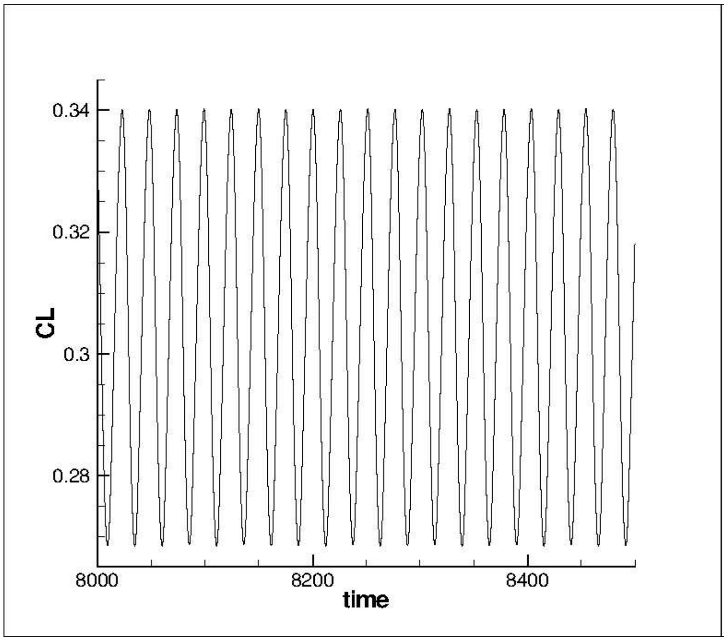

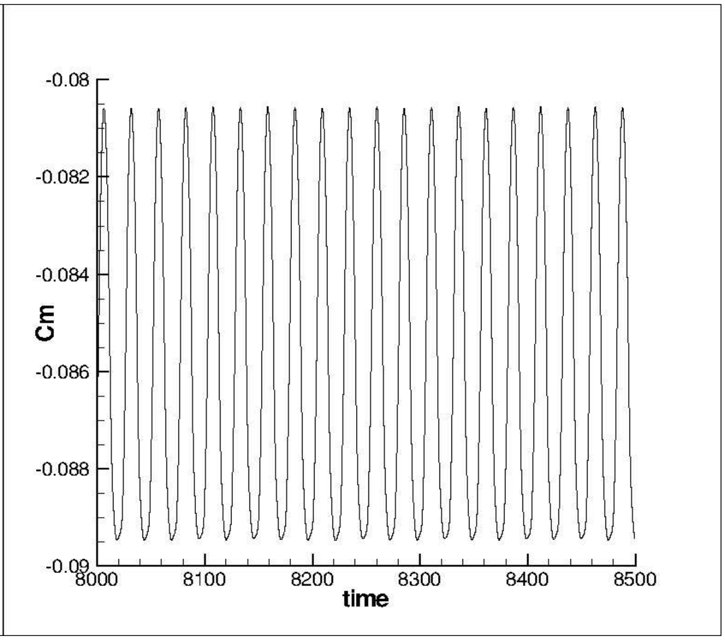

Figure 33: Lift coefficient predicted by DES ($AoA = 0.0°, \alpha_0 = 0.85°$)

Figure 34: Moment coefficient predicted by DES ($AoA = 0.0°, \alpha_0 = 0.85°$)

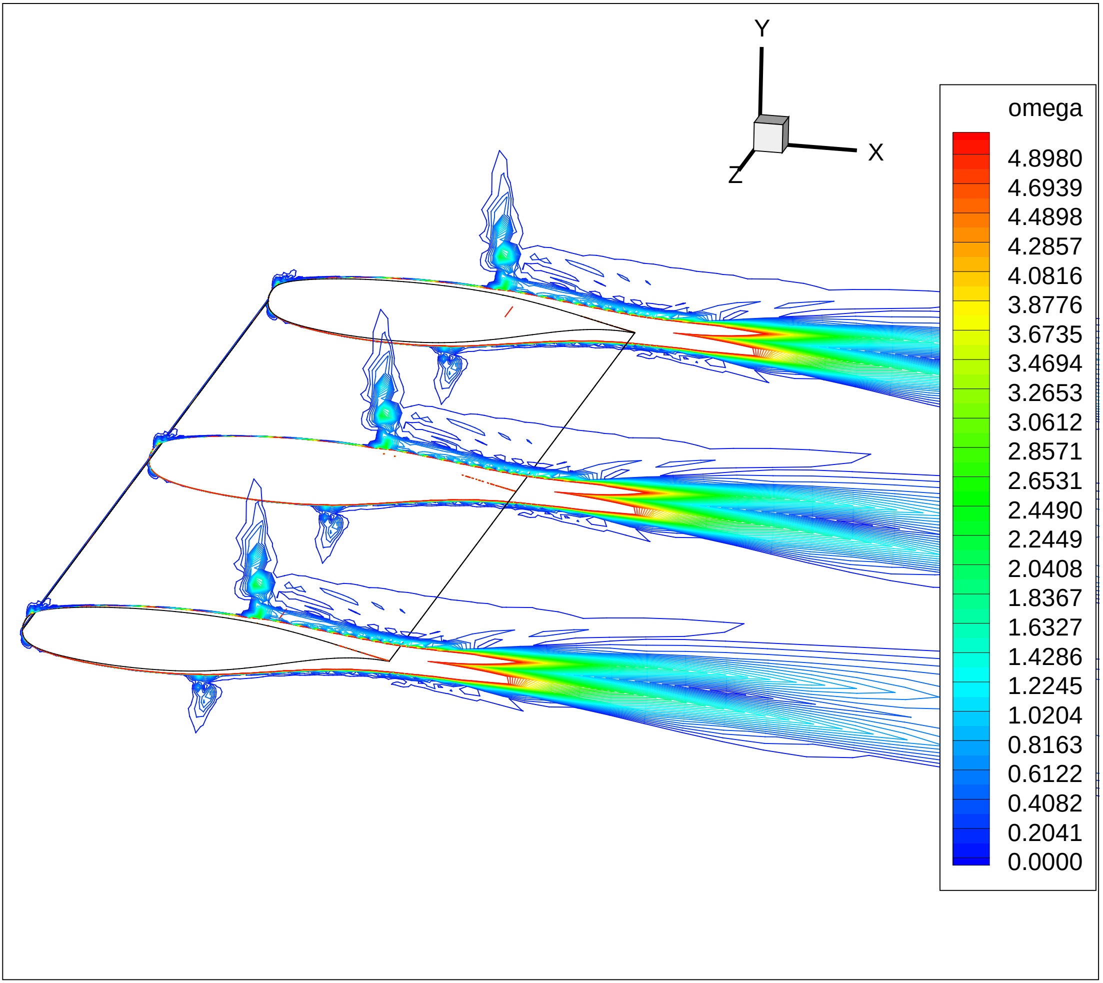

Figure 35: Instantaneous vorticity magnitude predicted by DES ($AoA = 0.0°, \alpha_0 = 0.85°$)